ARTICLE

Magnetic Response Combined with Bioactive Ion Therapy: A RONS-Scavenging Theranostic Nanoplatform for Thrombolysis and Renal Ischemia−Reperfusion Injury

Lian Xu, Ying Luo, Qianying Du, Wenli Zhang, Liu Hu, Ni Fang, Junrui Wang, Jia Liu, Jun Zhou, Yixin Zhong, Yun Liu, Haitao Ran, Dajing Guo,* and Jie Xu*

Cite This: https://doi.org/10.1021/acsnano.2c12091

Read Online

ACCESS | 📊 Metrics & More | 📄 Article Recommendations | 🆂🅸 Supporting Information

ABSTRACT: Currently, the limited efficacy of antithrombotic treatments is attributed to the inadequacy of pure drugs and the low ability of drugs to target the thrombus site. More importantly, timely thrombolysis is essential to reduce the sequelae of cardiovascular disease, but ischemia−reperfusion injury (IRI) remains a major challenge that must be solved after blood flow recovery. Herein, a multifunctional therapeutic nanoparticle (NP) based on Fe_3O_4 and strontium ions encapsulated in mesoporous polydopamine was successfully constructed and then loaded with TNK-tPA (FeM@Sr-TNK NPs). The NPs (59.9 min) significantly prolonged the half-life

of thrombolytic drugs, which was 3.04 times that of TNK (19.7 min), and they had good biological safety. The NPs were shown to pass through vascular models with different inner diameters, curvatures, and stenosis under magnetic targeting and to enable accurate diagnosis of thrombi by photoacoustic imaging. NPs combined with the magnetic hyperthermia technique were used to accelerate thrombolysis and quickly open blocked blood vessels. Then, renal IRI-induced functional metabolic disorder and tissue damage were evidently attenuated by scavenging toxic reactive oxygen and nitrogen species and through the protective effects of bioactive ion therapy, including reduced apoptosis, increased angiogenesis, and inhibited fibrosis. In brief, we constructed a multifunctional nanoplatform for integrating a "diagnosis-therapy-protection" approach to achieve comprehensive management from thrombus to renal IRI, promoting the advancement of related technologies.

KEYWORDS: thrombolysis, magnetic response, ischemia−reperfusion injury, reactive oxygen and nitrogen species, bioactive ion therapy
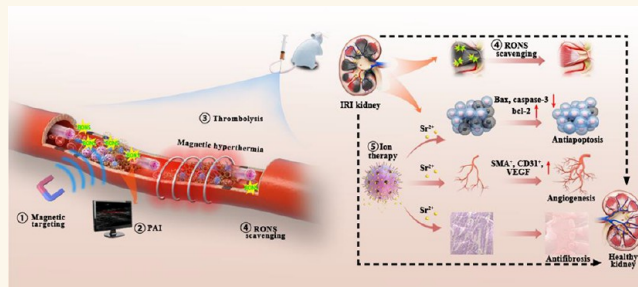
T hrombosis, as a global health problem, brings high mortality and huge economic pressure to the public. Currently, drug thrombolysis is the main clinical method for treating thrombi. However, due to the short half-life of single-drug thrombolytic therapy and the occurrence of unexpected bleeding complications, especially fatal cerebral hemorrhage, its effect is limited.[1,2] More importantly, the restoration of blood flow after thrombolysis does not indicate that the problem is resolved, and restoration of ischemia-tissue perfusion may provoke irreversible ischemia−reperfusion injury (IRI). IRI manifests as an ischemic injury that is further aggravated after blood perfusion is restored to the ischemic organ. In addition, ischemic stroke, traumatic shock, organ transplantation and surgery may cause IRI.[3,4] Therefore, how to rapidly treat thrombi to save ischemic tissue and prevent and treat IRI is the main challenge that must be solved.

The active targeting strategy is a promising approach for delivering nanoparticles (NPs) to specific thrombus targets.[5,6] Platelets and fibrin, the major components of thrombi, are commonly used targets for drug delivery. In our previous study, cyclic RGD peptides (targeting integrin $\alpha IIb\beta 3$ on platelet membrane surfaces),[7] EWVDV peptides (targeting platelet membrane surface P-selectin),[8,9] and CREKA peptides (targeting fibrin, existing in various types of thrombi)[10] were used to construct nanoprobes, achieving a good targeting effect
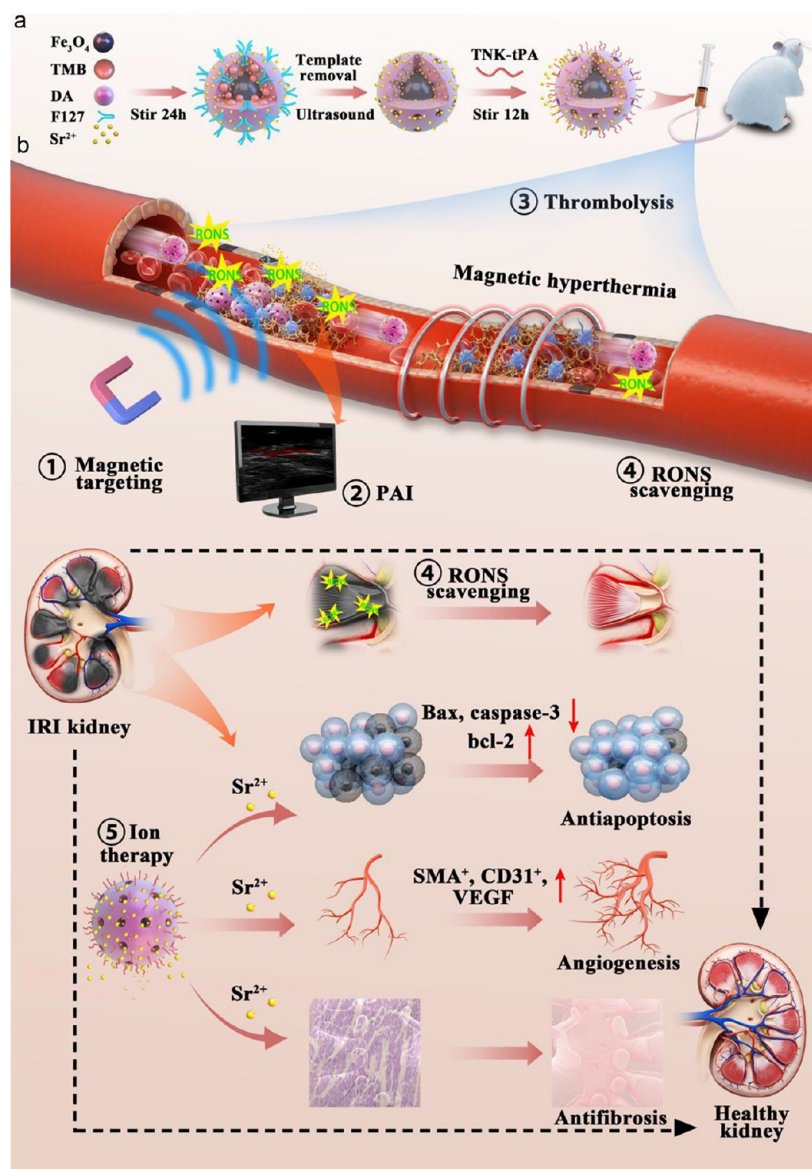
Figure 1. (a) Scheme for FeM@Sr-TNK NP synthesis. (b) Schematic diagram of FeM@Sr-TNK-mediated thrombolytic therapy, photoacoustic imaging, kidney protection, and RIRI treatment after thrombolysis.

on mural thrombi. However, with the deepening of research, we found that the targeting effect in occlusive thrombi is not satisfactory. The reason could be that the occluded thrombus leads to the termination of blood flow, and the number of nanoprobes that can reach the thrombus site is limited.

Thrombolytic drug-loaded NPs combined with external stimulation (such as heat, light, and magnetism) have great application prospects in imaging, drug delivery, and accelerating thrombolysis.[11−13] Among methods, magnetic targeting (MT) has shown great potential in the delivery of NPs to occluded thrombi because it can provide a driving force independent of blood flow, concentration, or pressure gradient.[14] It can realize long-distance, dexterous, precise, and fast drive and control of magnetic nanoparticles (MNPs).[14] More importantly, MNPs with a magnetocaloric response can facilitate drug release and local hyperthermia can reduce the dose of thrombolytic drugs and accelerate thrombolysis.[15−17] Liu et al. confirmed that the use of rt-PA at <20% of the conventional dose may achieve repeatable and

effective targeted thrombolysis under magnetic guidance.[18] Voros et al. showed that thrombus dissolution was significantly enhanced under alternating magnetic field heating.[19] In addition, with the continuous development of third-generation thrombolytic drugs, the level of targeting of tenecteplase (TNK-tPA) to thrombus fibrin is higher than that of other thrombolytic drugs, and the thrombolytic effect is significantly increased.[20] Inspired by this finding, the MT and magneto-caloric effect of Fe_3O_4 particles were combined with TNK-tPA to accelerate thrombolysis and quickly restore the reperfusion of ischemic tissue.

Although the rapid restoration of ischemic tissue reperfusion is an effective method to reduce infarct size, reperfusion may also cause IRI.[3] Reactive oxygen and nitrogen species (RONS) play important roles in IRI and cell structures such as proteins, and DNA can be seriously damaged by severe oxidative damage.[21] However, current diagnosis and treatment methods are not perfect, which will eventually lead to serious sequelae (such as brain sensory problems, loss of consciousness, motor
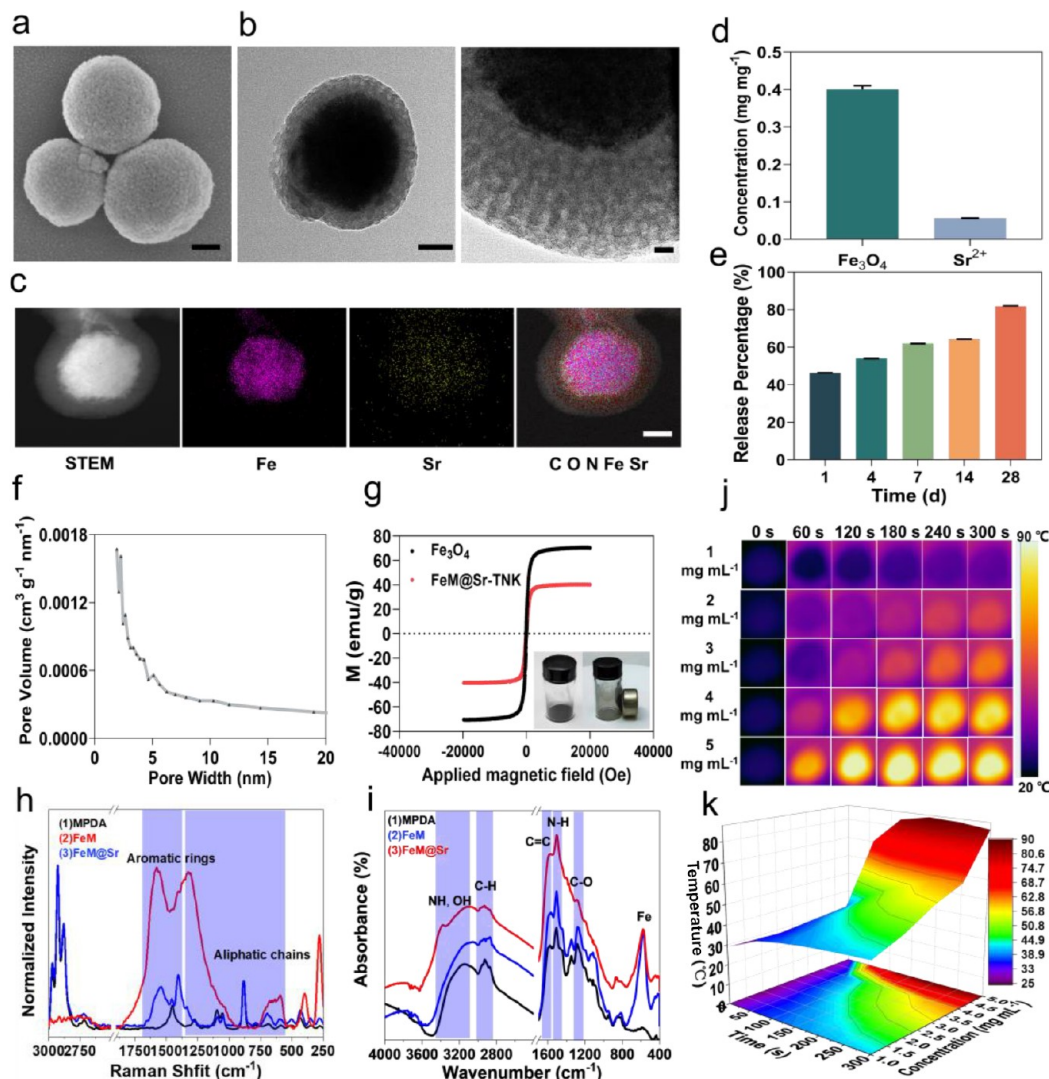
Figure 2. Characterization of FeM@Sr-TNK NPs and related materials. (a) SEM image of FeM@Sr-TNK NPs (scale bar: 100 nm). (b) TEM image of FeM@Sr-TNK NPs (scale bars: 100 nm; 20 nm). (c) STEM image and the elemental mapping of Fe, Sr and C, O, N, Fe, and Sr combined (scale bar: 100 nm). (d) The contents of Fe_3O_4 and Sr^{2+} in the FeM@Sr-TNK NPs measured by ICP-OES. (e) The percentages of Sr^{2+} released from FeM@Sr-TNK NPs on different days (1, 4, 7, 14, and 28 d). (f) Pore size distribution of FeM@Sr-TNK NPs. (g) Hysteresis loop test of Fe_3O_4 and FeM@Sr-TNK NPs. (Optical images of FeM@Sr-TNK NPs in the absence (left) and presence (right) of a magnet.) (h) Raman spectra and (i) FTIR absorption spectra of MPDA, FeM, and FeM@Sr NPs. (j) Thermal imaging and (k) 3D temperature map of the FeM@Sr-TNK NPs exposed to alternating magnetic fields from 0 to 5 min within the concentration range (1−5 mg mL^{-1}).

dysfunction, and heart arrhythmia) in patients as the prevention and treatment of IRI are missed.[3]

Currently, introducing antioxidant-based nanomedicine into the body is a mainstream way of addressing RONS for thrombotic disease.[22−24] Polydopamine (PDA), a mussel-inspired material, exhibits extensive antioxidative activities against a variety of toxic RONS, and the expression of inflammatory mediators and cytokines can be inhibited by PDA to decrease the inflammatory response triggered by RONS.[25−27] PDA-based NPs have been applied in treating various diseases related to oxidative stress, including ischemic stroke,[25] myocardium IRI,[26] acute lung injury,[28] acute kidney injury,[29] and Parkinson's disease.[30] In addition to its excellent antioxidant properties, PDA also has many biological functions, including strong chelating ability, strong adhesive properties, ability to easily functionalize, and good biocompatibility.[31] PDA has a wide range of optical absorption

capabilities, making it available for photoacoustic imaging (PAI)[31] and photothermal therapy (PTT).[32] Recently, encouraging progress has been made in the hierarchical structure and progressive assembly of PDA, and new nanostructures with better properties and functions have been constructed compared with those of simple NPs.[33] Among them, magnetic PDA has attracted much attention because of its magnetic response effect, including MT, magnetic hyperthermia (MH) and magnetic separation.[34,35] More importantly, a nanostructure of magnetic mesoporous PDA (MPDA), in addition to the above properties, also has greater capacity and a more flexible structure than PDA,[36] which has been applied in the fields of drug delivery,[37] tumor treatment,[38] bioassays,[39,40] and catalysis.[41,42] Therefore, we utilized these excellent properties of magnetic MPDA to construct a multifunctional diagnostic and therapeutic nano-platform with a magnetic response (including MT and MH),

high drug loading, and chelated strontium ions to achieve a seamless connection from thrombolysis and to realize the prevention and treatment of renal ischemia—reperfusion injury (RIRI).

In the past decade, many bioactive nanomaterials with unique biological activities have been used to treat different diseases and tissue regeneration.[43] Bioactive ions extracted from bioactive materials have advantages of low risk, low cost, and high stability and are widely used in regenerative medicine and tissue engineering.[44−46] The therapeutic functions of bioactive ions have been successfully verified, and these functions include improving cell growth and proliferation, stimulating angiogenesis, and enhancing anti-inflammatory activities.[47] Recently, methods of treating bioactive ions have been used to repair multiple damaged tissues, such as bone and adipose tissue.[48] Recent studies have proven that bioactive ions have therapeutic effects on myocardial infarction. Yi et al. demonstrated that silicon ions have a notable therapeutic effect on acute myocardial infarction by regulating cell behavior and angiogenesis, and "ion therapy" was used as a useful method to treat myocardial infarction.[49] Furthermore, Mao et al. proved that strontium ions could promote angiogenesis more than silicon ions in the process of bone regeneration.[50] Xing et al. used strontium-containing composite hydrogels to treat myocardial IRI in mice. The results showed that strontium ions could become a therapeutic element for damaged myocardial tissue and revealed the cardioprotective mechanism of strontium ions against IRI.[51] Therefore, in this experiment, we chelated strontium ions in MPDA to promote the angiogenesis of ischemic tissue and achieve the long-term treatment of RIRI repair.

To the best of our knowledge, magnetic MPDA, as a drug delivery system, has obvious advantages in thrombotic diseases, but there have been no reports of applications in related fields. More importantly, bioactive ion therapy is an emerging therapeutic modality, and strontium ions have proven useful for the treatment of myocardial IRI.[51] Considering the pathophysiological characteristics of thrombotic disease, in this research, we combined these two advanced strategies to construct Fe_3O_4@MPDA-Sr-TNK (FeM@Sr-TNK) NPs using MT to enrich NPs in thrombus tissue and acquire the PAI of thrombi. Furthermore, we used third-generation thrombolytic drugs combined with the magnetocaloric effect for efficient thrombolysis to quickly unblock the occluded blood vessels. When the ischemic tissue was restored to perfusion, FeM@Sr-TNK NPs played a protective role in scavenging RONS, treating RIRI, promoting vascular regeneration, and repairing damaged tissue (Figure 1b). In brief, we constructed a multifunctional nanoplatform for integrating a "diagnosis-therapy-protection" method to achieve comprehensive management of thrombi to treat RIRI.

RESULTS AND DISCUSSION

Characterization of FeM@Sr-TNK NPs. The process of synthesizing the FeM@Sr-TNK core—shell is illustrated in Figure 1a. The entire synthesis process included the following steps: preparation of the precursor (Fe_3O_4@PDA-Sr/F127/TMB), removal of the template to obtain Fe_3O_4@MPDA-Sr (FeM@Sr), and loading of TNK-tPA onto FeM@Sr to obtain the final FeM@Sr-TNK. As shown in Figure 2a, the obtained FeM@Sr-TNK NPs exhibited a complete spherical morphology, and an obvious core—shell structure was clearly observed by TEM (Figure 2b). The result of element line-scan mapping

proved the existence of Fe and Sr (Figure S1a,b). The elemental mapping images revealed that MPDA was coated uniformly onto the surface of Fe_3O_4, and Sr^{2+} was dispersed in MPDA (Figure 2c). Inductively coupled plasma-optical emission spectrometry (ICP-OES) was used to evaluate the Fe_3O_4 and Sr^{2+} contents in the FeM@Sr-TNK NPs, and the values were 0.4 ± 0.0082 mg mg^{-1} and 0.056 ± 0.00029 mg mg^{-1}, respectively (Figure 2d). The TNK loading rate was $24.6\% \pm 0.51$ (14.76 μg mg^{-1}). The drug loading rate of MDPA reported in the literature has varied greatly.[52−55] The following factors could affect the drug loading rate of MPDA: the nature of the drug itself, the size and length of the mesopores, a hollow structure, the connection mode between the drug and the MPDA, whether there is membrane coating, etc. The concentration of Sr^{2+} released from FeM@Sr-TNK NPs at different times (1, 4, 7, 14, 28 d) was determined by ICP, and the results revealed that with increasing time, Sr^{2+} was constantly released to ensure that the NPs exhibited a long-term treatment ability (Figure 2e). Then, the average diameters and average ζ potentials of Fe_3O_4@MPDA (FeM), FeM@Sr and FeM@Sr-TNK were measured. The diameters of FeM, FeM@Sr and FeM@Sr-TNK were 634.97 ± 4.01, 660.68 ± 1.52, and 684.13 ± 2.30 nm, respectively (Figure S2a). The ζ potentials of FeM, FeM@Sr and FeM@Sr-TNK were 9.45 ± 1.17 mV, -10.31 ± 0.48 mV and 29.14 ± 0.41 mV, respectively; thus, the potential significantly changed owing to every step of the synthesis (Figure S2b). Nitrogen adsorption—desorption of FeM@Sr NPs showed a type-IV isotherm with a type H3 hysteresis loop at $P/P_0 = 0.8−1.0$, demonstrating the existence of mesopores (Figure S3). In addition, the surface area and pore size of FeM@Sr NPs were calculated to be 8.16 m^2/g and 11.69 nm, respectively, indicating that a surface area was available for TNK loading. The broad distribution and peak at 2.0 nm should be attributed to the irregular mesoporous structure (Figure 2f). The saturation magnetization values of Fe_3O_4 and FeM@Sr-TNK NPs were found to be 70 and 40 emu g^{-1}, respectively, at an applied magnetic field of 3 kOe, which exhibited sufficient magnetization (Figure 2g). In addition, FeM@Sr-TNK NPs also showed mobility under the application of an external magnetic field.

To clarify the interaction between Fe_3O_4, MPDA, and Sr^{2+} and demonstrate the successful synthesis of FeM@Sr NPs, Raman spectroscopy and Fourier transform infrared (FTIR) spectroscopy were applied. New aromatic ring signal peaks at 1544, 1405, and 1336 cm^{-1} appeared in FeM, and the intensity was greatly enhanced compared with that of MPDA, which demonstrated that Fe_3O_4 interacted with MPDA. The characteristic peaks of aliphatic chains could be seen at 1453, 1097, and 1054 cm^{-1} in the spectra of MPDA, and they moved to 1457, 1094, and 1048 cm^{-1} in FeM. These movements were attributed to the interaction between Fe_3O_4 and MPDA, which proved that Fe_3O_4 already existed in FeM. The Raman spectra of PDA were similar to those previously obtained by Ma et al.[56] Comparing the Raman spectra of FeM@Sr and FeM, there were 1578 and 1306 cm^{-1} new aromatic ring signal peaks in FeM@Sr, respectively, and the intensity here was greatly enhanced compared with FeM, proving that Sr^{2+} interacted with MPDA.[57] At the same time, the characteristic peaks of aliphatic chains at 1544, 1405, and 1335 cm^{-1} in the spectrum of FeM moving to 1555, 1408, and 1326 cm^{-1} in FeM@Sr demonstrated that Sr^{2+} was successfully adsorbed on FeM (Figure 2h). As shown in Figure 2i, based on the basis of a
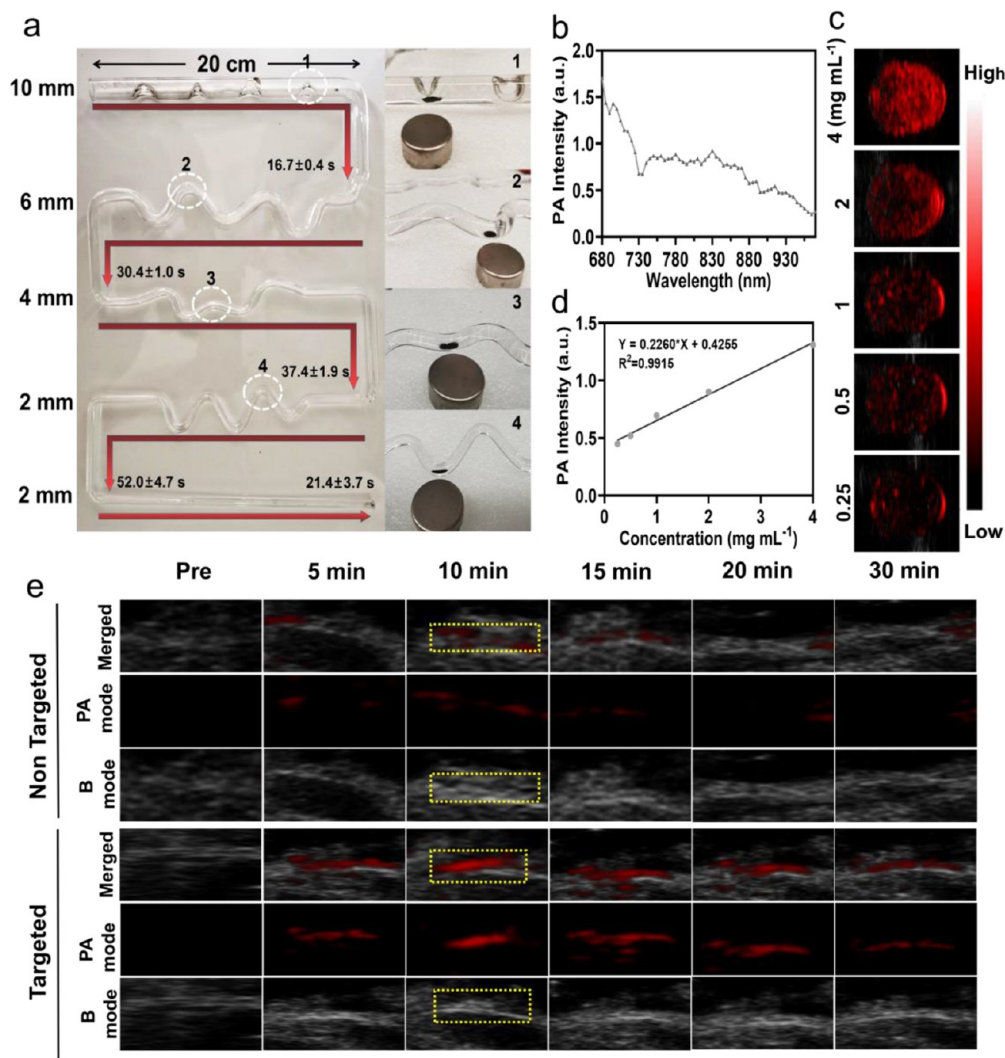
Figure 3. Targeting and imaging *in vitro* and *in vivo*. (a) MT ability of FeM@Sr-TNK NPs in a vascular model with different inner diameters, levels of stenosis, and torsion degrees. (b) PA signal change in FeM@Sr-TNK NPs in the wavelength range of 680−970 nm. (c) Corresponding PAI at a wavelength of 695 nm of FeM@Sr-TNK NPs at various concentrations. (d) Quantitative analysis of the corresponding signal intensity *in vitro*. (e) PAI of two groups (nontargeted group; targeted group (MT)) at diverse time points *in vivo* (thrombus region in dotted box).

previous study,[58,59] the absorption band at 583 cm^{-1} was attributed to the Fe−O vibration, and the absorption band changed from 1578 and 1284 cm^{-1} to 1567 and 1280 cm^{-1}, respectively, further demonstrating that Fe_3O_4 was successfully adsorbed on MPDA. The interaction between Sr^{2+} and the C=C and C−O of MPDA was demonstrated by the absorption bands at 2871, 1567, and 1280 cm^{-1} changing to 2929, 1569, and 1285 cm^{-1}, respectively. Both the infrared and Raman peak shifts were caused by adsorption, and these results were sufficient to demonstrate the successful construction of NPs. Moreover, an N 1s peak consistent with the pyrrolic nitrogen of PDA and an individual Sr 3d peak appeared in the X-ray photoelectron spectroscopy spectrum of FeM@Sr NPs (Figure S4a−c), which confirmed the formation of PDA shells on the surfaces of the Fe_3O_4 NPs[60] and successful loading of Sr^{2+}. With the stability of NPs verified (Figure S5), FeM@Sr-TNK NPs were uniformly dispersed in ethanol without obvious precipitation at different times (1, 7, 14, and 28 d). As the basis for thermosensitive thrombolysis, the MH performance of FeM@Sr-TNK NPs in this study was verified.

The significant changes in the temperature of FeM@Sr-TNK NPs increased under the stimulation of alternating magnetic fields. Following this increase, the temperature maps of concentration-dependent FeM@Sr-TNK NPs were captured by an infrared camera (Figure 2j). When the concentration was 1−5 mg mL^{-1}, the temperature rose to 41.9−84.2 °C within 5 min (Figure 2k). As shown in Figure S6, the temperature of the Fe_3O_4 group, FeM@Sr NP group, and FeM@Sr-TNK NP group increased to nearly 90 °C, but the PBS group and the MPDA group did not increase significantly.

Targeting and Imaging *In Vitro* and *In Vivo*. Effectively delivering NPs to the thrombus site and visualizing the thrombus are vital in diagnosing and treating thrombotic diseases. MT is a promising direction for delivering NPs to thrombi; therefore, the effective magnetically guided capacity of FeM@Sr-TNK NPs was demonstrated. As shown in Figure 3a, FeM@Sr-TNK NPs smoothly passed through the blood vessel models with inner diameters ranging from coarse to fine (10, 6, 4, 2 mm), with different curvatures and stenosis under MT, indicating that FeM@Sr-TNK NPs have the potential to
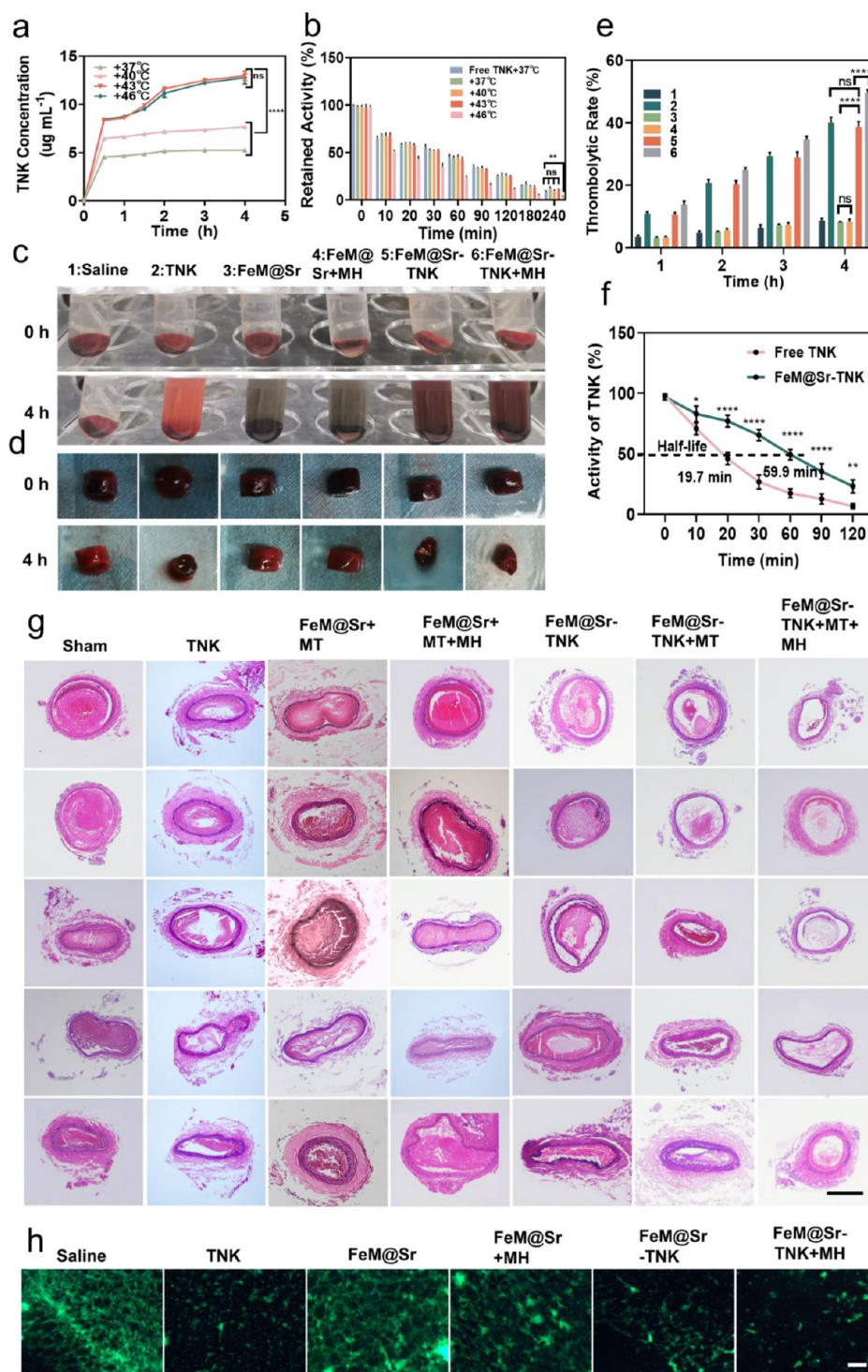
Figure 4. Accelerated thrombolytic therapy was performed *in vitro* and *in vivo*. (a) Concentration changes of TNK released from FeM@Sr-TNK NPs at different temperatures and times, ns: not significant, ****$p < 0.0001$ versus the 43 °C group. (b) *In vitro* enzymatic activity of free TNK+37 °C and FeM@Sr-TNK preparations determined at 37 °C, 40 °C, 43 °C, and 46 °C, ns: not significant, *$p < 0.05$ versus the free TNK+37 °C group. (c) The supernatant of the thrombolysis processes before and 4 h after being treated with saline, TNK, FeM@Sr, FeM@Sr+MH, FeM@Sr-TNK and FeM@Sr-TNK+MH. (d) Blood clots and related thrombolytic rate (e) after treatment with saline, TNK, FeM@Sr, FeM@Sr+MH, FeM@Sr-TNK and FeM@Sr-TNK + MH at different time points. (f) Enzyme activity−time curve in plasma after intravenous injection of free TNK or FeM@Sr-TNK into rats. (g) H&E staining of the thrombi in the renal arteries after different treatments (scale bar: 200 μm). (h) Fluorescence microscopy images of fibrin clots with different treatments (scale bar: 100 μm).

be applied to different levels of blood vessels or plaque-containing vessels. Moreover, the high delivery rate of 80 ± 6.7% in the blood vessel models *in vitro* demonstrated the potential of NPs in vascular diseases.

Given the excellent photoacoustic signal of polydopamine,[61] FeM@Sr-TNK NPs were investigated by using a Vevo LAZR PAI system. Based on the result of a peak at 695 nm, we chose 695 nm for use in subsequent PAI research (Figure 3b). As

seen in Figure 3c,d, the FeM@Sr-TNK NPs exhibited photoacoustic (PA) signals, and their signal intensity was dependent on their concentration. Then, we studied the PAI ability of FeM@Sr-TNK NPs *in vivo*. The PA signal could be seen in the right renal artery area 5 min after administration in both groups, and the signal intensity of the targeted group was notably higher (Figure 3e). The highest PA signal appeared at 10 min after injection, and the clear signal was much stronger than that in the nontargeted group from 10 to 20 min, which implied that FeM@Sr-TNK NPs could rapidly target thrombi under MT. The signals of the two groups were gradually reduced at 30 min (Figure S7). PAI with high sensitivity can be used to detect thrombi and monitor the progress of thrombolysis, which lays a foundation for the rapid diagnosis and treatment of thrombi.

Thrombolytic Therapy *In Vitro* and *In Vivo*. According to a previous study, 60% of initially loaded tPA was released into the surrounding solution after 24 h at 42 °C instead of 30% at 37 °C.[19] The cumulative release of TNK in serum was determined at 37 °C, 40 °C, 43 and 46 °C using an enzyme-linked immunosorbent assay (ELISA). Compared to the initial release at 30 min, the cumulative release was 8.34 μg mL^{-1} at 43 °C, which was similar to that at 46 °C and much more than that at 37 and 40 °C. During the observation period, a plateau emerged at 37 and 40 °C, and sustained release behavior occurred at 43 and 46 °C, in which the cumulative release at 180 min reached 13.14 μg mL^{-1} and 12.77 μg mL^{-1}, which were much higher than those at 37 and 40 °C (5.27 μg mL^{-1} and 7.67 μg mL^{-1}) (Figure 4a). The enzymatic activity of free TNK+37 °C and TNK from FeM@Sr-TNK NPs at 37 °C, 40 °C, 43 °C, and 46 °C was determined by the chromogenic substrate S-2288.[62] The activity of TNK decreased gradually over time. After 4 h, the drug activity of the 46 °C group decreased significantly (3.94%), which was lower than that of the other four groups (Figure 4b). Therefore, to obtain high drug release and high activity, according to the results of drug release and activity, we chose 43 °C as the best temperature for the follow-up experiment.

The thrombolytic efficiency *in vitro* was calculated by the blood clots of rats. Figure S8 is a corresponding quantitative figure to Figure 4c, which shows the color changes, and at 4 h after treatments, the amounts of hemoglobin in the supernatant of blood clot showed similar trends with the dissolution efficiencies. With dissolution, when clots were treated with a single TNK, FeM@Sr-TNK, or FeM@Sr-TNK+MH, all clots gradually dissolved into smaller sizes. In contrast, the clots treated with saline, FeM@Sr, or FeM@Sr+MH barely lysed after 4 h of treatment (Figure 4d). The dissolution efficiencies of the clots were quantified by performing measurements at 1, 2, 3, and 4 h after treatments. The clots treated with FeM@Sr-TNK exhibited a similar dissolution efficiency (approximately 38.7%) to those treated with a single TNK (approximately 40%), which was higher than those obtained with saline, FeM@Sr, or FeM@Sr+MH treatments (8.7%, 8.2%, and 8.4%, respectively). Moreover, the low dissolution efficiency in the FeM@Sr+MH group also showed that the thrombolytic effect could not be achieved by MH alone. Obviously, FeM@Sr-TNK+MH treatment achieved the highest dissolution efficiency (approximately 49.5%), which indicated that the FeM@Sr-TNK association with MH accelerated blood clot lysis (Figure 4e).

TNK is a fibrinolytic enzyme that decomposes blood clots through fibrinolysis. The fibrinolytic activity of FeM@Sr-TNK NPs with MH was investigated by a fibrin clot model. As shown in Figure S9a, to visually monitor the degree of fibrin lysis, the diameter and area of the lysis ring around each sample well were measured. Figure S9b shows that the small lysis ring area attributed to FeM@Sr+MH was similar to that attributed to saline and FeM@Sr NPs. The area of the lysis ring attributed to FeM@Sr-TNK NPs (0.502 ± 0.088 cm^2) was smaller than that attributed to TNK (0.946 ± 0.140 cm^2), which could be ascribed to incomplete TNK release. However, when FeM@Sr-TNK NPs were treated with MH, the degree of fibrin lysis (1.061 ± 0.088 cm^2) was similar to that of the free TNK group, indicating that the TNK encapsulated in the NPs retained its activity.

After intravenous injection of free TNK and FeM@Sr-TNK NPs, the enzyme activity−time curves of TNK are shown in Figure 4f. FeM@Sr-TNK NPs (59.9 min) significantly prolonged the half-life of the thrombolytic drugs, which was 3.04 times that of free TNK (19.7 min). Moreover, free TNK was almost completely cleared after 2 h of administration, while in the FeM@Sr-TNK NP group, approximately 20% of the initial dose was still retained. These results indicated that FeM@Sr-TNK NPs not only retained special activity but also prolonged the circulation time of TNK *in vivo*.

Performing thrombolysis with occluded thrombi is a challenge, as drug delivery is inefficient *in vivo*. In this study, an occlusive thrombus model was established to study the thrombolytic effect of FeM@Sr-TNK NPs. We examined the antithrombotic ability *in vivo* via histological examinations. Previous research has confirmed the higher targeting ability of TNK to thrombi and the high fibrin binding rate.[63] Additionally, the thrombus-targeted fibrinolysis of biocompatible NPs was represented by their preferential localization, effective thrombolysis, and improved safety of fibrinolytic drug dosage.[64] We used an infrared thermal imager to observe the temperature of the thrombus site. The thermal imaging results showed that the temperature of the targeted group could rise to 43 °C at 10 min and be maintained continuously; however, in the nontargeted group, the temperature rose to 39 °C at most at 10 min and did not exceed 40 °C later. (Figure S10). Notably, in our study, H&E-stained sections showed that the fibrin net decreased, resulting in the shedding of platelets and red blood cells, which indicated that the FeM@Sr-TNK NPs exhibited great fibrinolytic ability with MT and MH (Figure 4g). As seen in Figure S11, compared with the sham group (thrombus residual rate: 88.5%), FeM@Sr+MT group (thrombus residual rate: 81.3%), and FeM@Sr+MT+MH group (thrombus residual rate: 81.4%), the FeM@Sr-TNK NP group showed better antithrombotic efficiency (thrombus residual rate: 46.54%), similar to that of TNK at the same dose (thrombus residual rate: 46.22%). Moreover, magnetic guiding-induced movement of the NPs aggregated at the thrombus site so that the FeM@Sr-TNK NPs+MT group achieved a better thrombolytic effect (thrombus residual rate: 34.38%), and compared with the single drug group, the residual rate of thrombus was reduced by 11.84%. What's more, treatment with the FeM@Sr-TNK NPs+MT+MH significantly accelerated the dissolution of the thrombus (thrombus residual rate: 11.04%), and the thrombus residual rate was reduced by 35.18% compared with that of the single TNK group. The above results indicated that pure MH therapy would not achieve a significant thrombolytic effect. In contrast, MT and local hyperthermia-induced TNK release was a quite effective and accurate strategy compared to that of NPs
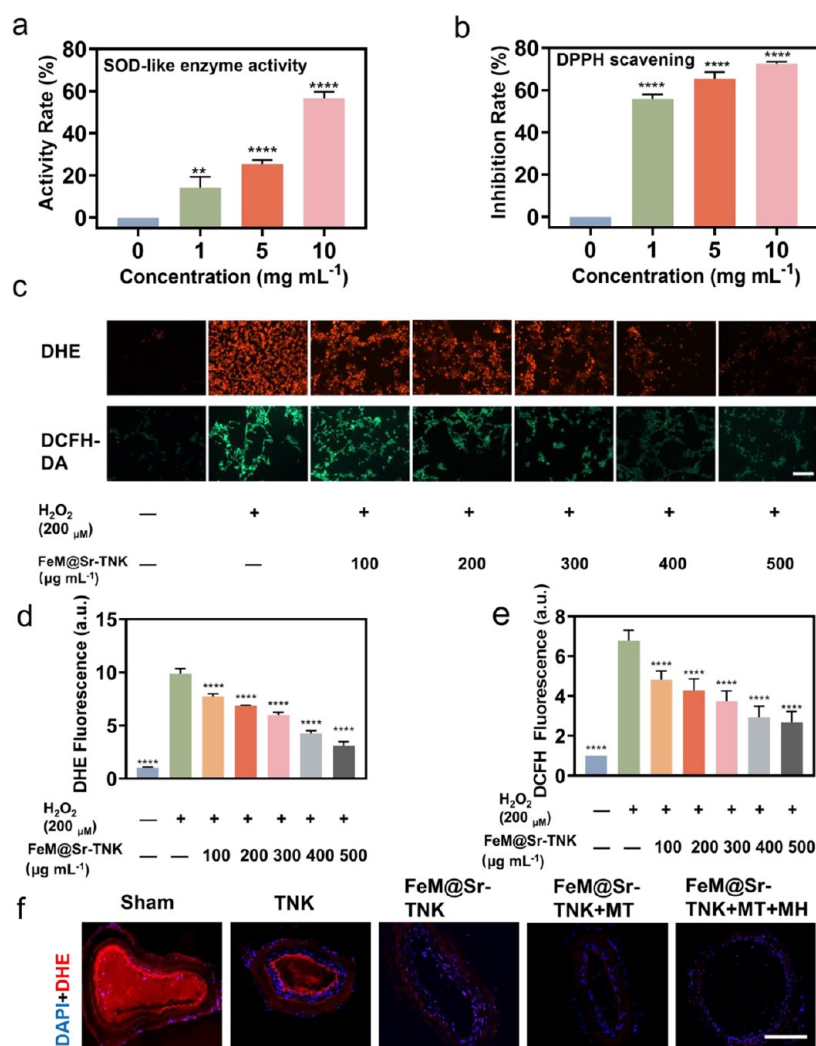
Figure 5. Antioxidant enzymatic activity *in vitro*. The ability of SOD-like enzyme (a) and scavenging DPPH (b) of FeM@Sr-TNK NPs at different concentrations. (c) DHE and DCFH-DA staining images of HEK293 cells stimulated with H_2O_2 (200×10^{-6} M) and FeM@Sr-TNK NPs (scale bar: 100 μm). (d) DHE levels and (e) DCFH-DA levels, ****$p < 0.0001$ versus the H_2O_2 control group. (f) DHE-DAPI staining of the right renal artery thrombus after different treatments (scale bar: 200 μm).

without a controlled release design or single TNK, and the thrombolytic efficiency was significantly improved, suggesting the feasibility of targeted hyperthermia thrombolysis in the treatment of thromboembolic diseases. After treatment with FeM@Sr-TNK NPs+MT+MH, the temperature of the liver reached approximately 41 °C but the temperature of the spleen and kidney was only approximately 35 °C, which could be due to the uptake capacity of the liver (Figure S12).

To further clarify the site of the thrombolysis action of FeM@Sr-TNK NPs, fluorescein isothiocyanate (FITC)-labeled fibrin clots with different treatments were studied. As shown Figure 4h, the fibrin clots were not damaged in the saline, FeM@Sr, or FeM@Sr+MH groups. However, the fibrin network structure treated with FeM@Sr-TNK NPs was partly disintegrated. Moreover, after treatment with TNK and FeM@Sr-TNK NPs+MH (43 °C), the fibrin network structure was totally destroyed, leaving some broken skeletons and small fragments, showing that the dissolution of thrombi by FeM@Sr-TNK NPs+MH was achieved by decomposing the fibrin network.

RONS Scavenging *In Vitro* and at the Thrombus Site. The antioxidant system maintains a delicate balance between the production of RONS and the inactivation of RONS.[65] In fact, antioxidants and enzymes in the human body can inhibit the excessive generation of RONS. Nevertheless, these antioxidant defense systems are overloaded under IRI.[65] Thus, scavenging RONS and performing thrombolysis simultaneously may be a promising method to prevent and treat IRI. Since $O^{2\bullet-}$ is a major and toxic ROS and reactive nitrogen species (RNS) are involved in the development and progression of many diseases, we examined SOD-like enzyme activity and the ability to scavenge 1,1-diphenyl-2-picrylhydrazyl (DPPH) using testing kits. As shown in Figure 5a, we observed enzyme activity by FeM@Sr-TNK NPs that was concentration dependent, and a successful activity of $56.58 \pm 7.36\%$ at 10 mg mL^{-1} was obtained. Moreover, FeM@Sr-TNK NPs scavenged $72.5 \pm 4.74\%$ of DPPH at 10 mg mL^{-1} (Figure 5b). The corresponding color reaction also showed that the NPs had a good scavenging ability (Figure S13a-b). These results confirmed that the FeM@Sr-TNK NPs possess admirable antioxidative activities toward RONS *in vitro*.

Oxidative stress plays a vital role in the pathogenesis of IRI injury. In view of the powerful ability of FeM@Sr-TNK NPs to scavenge RONS, we used fluorescein-labeled dihydroethidium
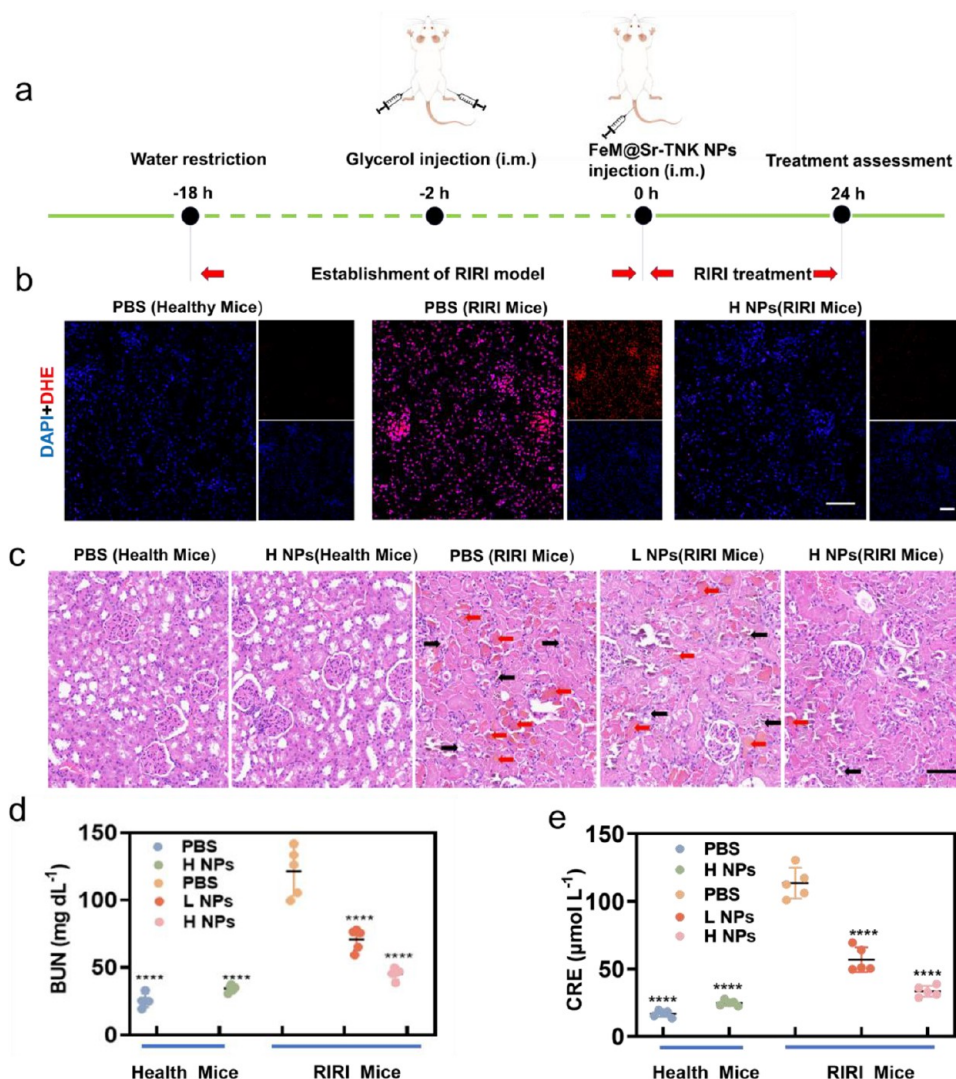
Figure 6. Construction of the RIRI model and its treatment with FeM@Sr-TNK NPs. (a) Establishment of the RIRI model and its relationship with treatment with FeM@Sr-TNK NPs. (b) Images of DHE- and DAPI-stained kidney tissue from healthy mice and RIRI mice treated with PBS or FeM@Sr-TNK NPs (scale bar: 100 μm). (c) Kidney tissue images of healthy mice and RIRI mice with H&E staining treated with PBS or FeM@Sr-TNK NPs. (The black arrow-damaged kidney tubules; the red arrow-cast formation.) (scale bar: 100 μm). (d) BUN and (e) CRE in healthy mice and RIRI mice treated with PBS or FeM@Sr-TNK NPs. L NP group: 200 μL/mouse; H NP group: 800 μL/mouse (4 mg mL^{-1} FeM@Sr-TNK NPs).

(DHE) and 2,7-dichlorodihydrofluorescein diacetate (DCFH-DA) probes for detection. Significantly increased fluorescence indicated that HEK293 cells produced high levels of ROS under hydrogen peroxide induction. As shown in the experimental groups, we confirmed that no excessive ROS existed in HEK293 cells after FeM@Sr-TNK NPs were added. Moreover, the cells pretreated with FeM@Sr-TNK NPs at various concentrations exhibited decreased fluorescence intensities of DHE and DCFH-DA (Figure 5c). Quantitative analysis results showed that FeM@Sr-TNK NPs significantly reduced ROS levels in HEK293 cells, and the higher the concentration of FeM@Sr-TNK NPs, the lower the fluorescence density (Figure 5d,e). The apparent effects of FeM@Sr-TNK NPs on the suppression of nitric oxide (NO) induced by lipopolysaccharide (LPS) in HEK293 cells were also observed. As shown in Figure S14, FeM@Sr-TNK NPs were used to successively scavenge NO. Furthermore, only the H$_2$O$_2$-stimulated group had obvious cell death, but the cell

survival rate after the FeM@Sr-TNK NP treatment increased significantly (Figure S15).

After thrombosis, damaged endothelial cells and activated platelets will produce additional ROS, which will promote thrombosis when ROS continue to increase.[66] Therefore, scavenging excessive ROS at the thrombus site is necessary during the treatment process. The ability of FeM@Sr-TNK NPs to clear ROS at thrombotic sites was verified by DHE staining (Figure 5f). There was obvious DHE fluorescence in the sham group, indicating that there was a large amount of ROS at the thrombotic site. Due to the antioxidant activity of MPDA NPs, the last three groups almost completely cleared all ROS. The FeM@Sr-TNK NPs+MT+MH group significantly suppressed ROS generation, suggesting that the FeM@Sr-TNK NPs passively targeted the embolized vessel and exerted highly potent antioxidant effects (Figure S16).

RIRI Treatment *In Vivo*: RONS Scavenging in the Kidney Protects Renal Tubules and Improves Renal Function. RONS is among the critical targets that prevent
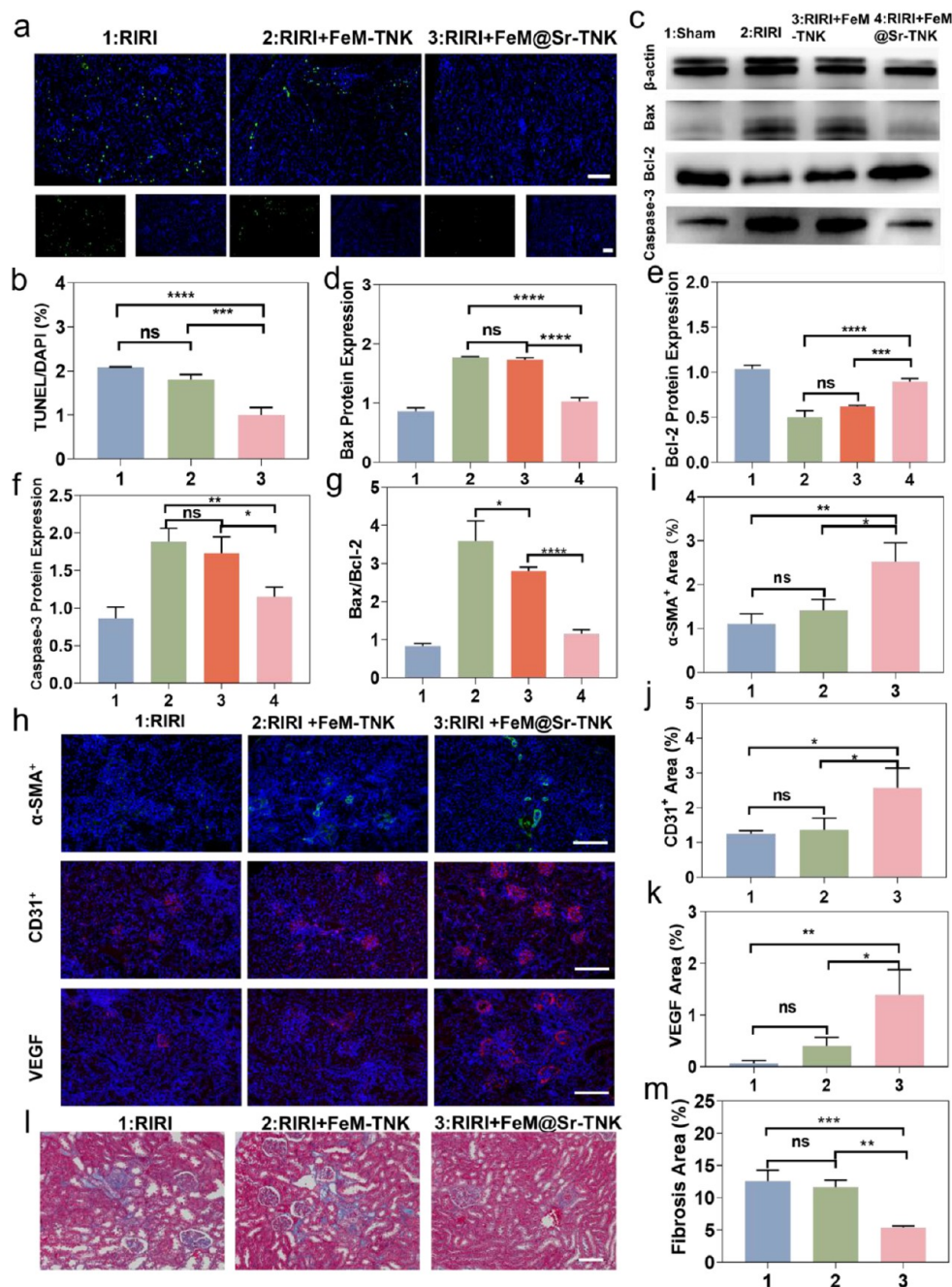
Figure 7. FeM@Sr-TNK NPs reduce nephrocyte apoptosis, increase angiogenesis, and inhibit renal fibrosis. (a,b) Representative and quantified staining of TUNEL$^+$ renal cells in the damaged area at day 3 after RIRI (green: TUNEL, blue: DAPI; scale bars: 50 μm). (c−g) Representative and averaged Western blot analysis for β-actin, bax, bcl-2, and caspase-3 in damaged renal tissues at day 3 after RIRI. (h-k) 28 days after RIRI, images and quantification of α-SMA$^+$ (green) blood vessels, CD31$^+$ (red) cells, and VEGF (red) in the damaged kidney area (scale bars, 100 μm). (l,m) Representative images and quantitative data of the damaged renal area dyed with Masson's trichrome at day 28 after RIRI. (Blue: collagen fibers, red: muscle fibers; scale bars: 100 μm).

RIRI. The RONS generated based on the basis of reoxygenation to ischemic tissues was considered to cause damage and trigger a series of harmful cellular reactions.[67] Thus, to further assess the RONS scavenging ability of FeM@Sr-TNK NPs for RIRI *in vivo*, DHE staining of renal tissue was performed. As shown in Figure 6a,b, FeM@Sr-TNK NPs had strong antioxidant defense ability in RIRI treatment. This shows that removing overexpressed RONS in ischemic tissue is an effective short-term prevention and treatment method for RIRI. In addition, the renal tissues of RIRI mice treated with

PBS were severely damaged, while other groups treated with FeM@Sr-TNK NPs alleviated renal injury in RIRI mice (Figure 6c). By analyzing the blood urea nitrogen (BUN) and creatinine (CRE) levels, we verified that FeM@Sr-TNK NPs could restore the renal function of RIRI mice (Figure 6d,e). As shown, RIRI mice treated with PBS showed elevated levels of BUN and CRE, which was a sign of renal failure. It was noteworthy that the FeM@Sr-TNK-treated group significantly reduced the BUN and CRE levels of RIRI mice, and there was
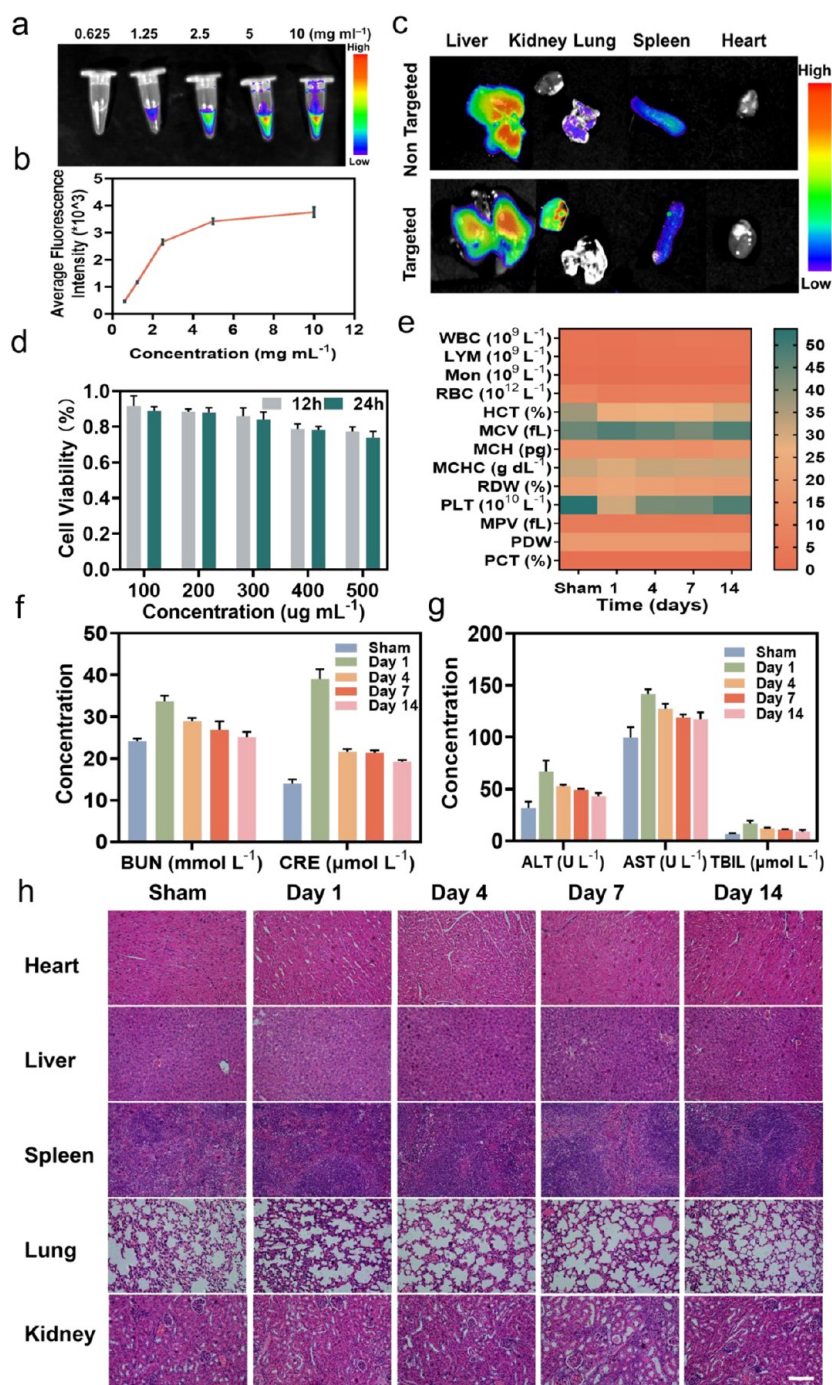
Figure 8. Toxicity assessments of the FeM@Sr-TNK NPs *in vitro* and *in vivo*. (a–c) *In vitro* FL images and fluorescence intensity of DIR-FeM@Sr-TNK. *Ex vivo* FLI of major organs. (d) Relative viabilities of HEK293 cells with different treatments at 12 and 24 h. (e) Whole-blood parameters in the mice treated with PBS or FeM@Sr-TNK NPs. (f) Serum levels of BUN and CRE in mice. (g) Serum levels of ALT, AST and TBIL in mice. (h) Organ images of healthy mice with H&E staining treated with PBS or FeM@Sr-TNK NPs (1 mg/mouse) (scale bar: 50 μm).

no notable difference between the RIRI mice treated with a high dose and healthy mice.

Bioactive Ion Therapy *In Vivo*: Reducing Apoptosis, Increasing Angiogenesis, and Inhibiting Fibrosis. Inevitably, tissue ischemia and reperfusion injury will cause different degrees of damage to ischemic organs. Bioactive ions, an emerging therapeutic modality, are gradually attracting attention. Accumulating research has shown that bioactive ions can induce specific cell reactions, affect the interaction between

cells, and promote the formation or regeneration of tissues and organs.[47]

To verify the bioactive ion therapy effect of NPs in protection and restoration after RIRI, we implemented multiple histological analyses. At day 3 after RIRI, the number of terminal deoxynucleotidyltransferase-mediated dUTP-biotin nick end labeling[+] (TUNEL[+]) nephrocytes detected in renal tissue was significantly more reduced after treatment with FeM@Sr-TNK than after the other two treatments (Figure

7a,b). Bcl-2 is an inhibitor of apoptosis, and Bax promotes apoptosis; these two proteins affect the process of apoptosis by interacting. Apoptosis was positively correlated with the ratio of Bax/Bcl-2, and the larger the Bax/Bcl-2 ratio, the higher the apoptosis rate. The caspase protein family plays an important role in the process of apoptosis. As the executor of apoptosis, caspase-3 is the key protease activated by various apoptosis-stimulating factors.[68] In this study, we observed that Bax and Caspase-3 protein expression decreased significantly, while Bcl-2 protein expression increased in the FeM@Sr-TNK group compared to the RIRI and FeM-TNK groups, showing that the FeM@Sr-TNK NPs reduced nephrocyte apoptosis (Figure 7c). The three corresponding protein expression levels and Bax/Bcl ratios showed a trend (Figure 7d−g). Moreover, to confirm the angiogenesis ability of FeM@Sr-TNK NPs, the amount of α-smooth muscle actin-positive (α-SMA$^+$) blood vessels, CD31$^+$ cells, and VEGF in renal tissue was detected on the 28th day after RIRI (Figure 7h). More green areas (α-SMA$^+$ blood vessels) (Figure 7i) and red areas (CD31$^+$ cells) (Figure 7j) were detected in the renal sections of the FeM@Sr-TNK group than in the RIRI control and FeM-TNK groups, indicating that more arterioles and blood capillaries increased. In addition, the results of immunofluorescence staining showed that the VEGF level (red) increased in the glomeruli of the FeM@Sr-TNK group on the 28th day after RIRI (Figure 7k). The formation of renal fibrosis was observed in all mice on the 28th day after RIRI, as analyzed by Masson trichrome staining, while the blue collagen fibers in the renal fibrosis area in the FeM@Sr-TNK group were smaller than those in the RIRI and FeM-TNK groups, demonstrating the potential antifibrotic ability of FeM@Sr-TNK NPs (Figure 7l,m). These data indicated that FeM@Sr-TNK NPs protected renal function after RIRI by inhibiting nephrocyte apoptosis, promoting blood vessel formation and reducing renal fibrosis. To verify the metabolism of Sr^{2+} in the kidneys, as shown in Figure S17, the concentration of Sr^{2+} in the kidneys of mice was detected at different points in time. The results showed that the Sr^{2+} concentration was 293.34 ± 8.98 μg g^{-1} at day 1 and 119.97 ± 8.17 μg g^{-1} at day 7, but the concentration of Sr^{2+} decreased significantly at days 14 (8.17 ± 0.55 μg g^{-1}) and 28 (0.16 ± 0.05 μg g^{-1}). This outcome suggested that Sr^{2+} could accumulate in the kidney for a certain period of time and could be cleared after a long time.

Biodistribution and Biosafety Assessment. Fluorescence imaging (FLI) was used for visual detection of the in vivo aggregation and biodistribution of FeM@Sr-TNK. As shown in Figure 8a,b, with increasing concentration in vitro, the fluorescence (FL) signal of DIR-FeM@Sr-TNK constantly increased and approached balance, and the same result was visually displayed by the quantitative analysis of FL. Twelve hours after administration, FLI was performed after removal of major organs, and the FL signals of kidneys in the targeted group were stronger than those in the nontargeted group; nevertheless, FL signals of other organs in the two groups were similar (Figure 8c). This outcome shows that the DIR-FeM@Sr-TNK NPs can target specific regions under magnetic navigation.

There was no erythrolysis in the different concentrations of FeM@Sr-TNK groups (1−5 mg mL^{-1}); however, a large amount of red solution appeared in the water group due to red blood cell damage. These results verified that the FeM@Sr-TNK NPs had good biological compatibility and reliability of detection in vivo (Figure S18). When different concentrations

of FeM@Sr-TNK NPs were cultivated with HEK293 cells for 12 or 24 h, the number and shape of cells were well preserved and the cell viability was approximately 80%. The results showed that in the proper concentration and time range, NPs did not cause damage to normal cells (Figure 8d).

The tail bleeding test showed that the bleeding time of the PBS group and FeM@Sr-TNK group was notably shorter than that of the TNK group, which indicated that the bleeding risk of the FeM@Sr-TNK group was lower than that of the TNK group and was acceptable compared to that of the PBS group (Figure S19a). Coagulation time refers to the time from when blood leaves blood vessels until it coagulates in vitro. Compared with the four experimental groups, although the anticoagulation effect of the FeM@Sr-TNK group was slightly different from that of PBS, it did not increase significantly in value; therefore, it was acceptable (Figure S19b).

To evaluate the safety of FeM@Sr-TNK NPs in vivo, we verified mice treated with numerous treatments were verified. The renal function, liver function, or hematological indices in the FeM@Sr-TNK group were not significantly damaged, showing that NPs had no obvious toxicity (Figure 8e−g). Additionally, there were no adverse side effects after FeM@Sr-TNK NP administration, as observed by H&E staining. Moreover, the characteristics of the treated groups were all similar to those observed for the control group (Figure 8h). In addition, by observation of the blood vessel walls in each group, the MH treatment groups did not show significant differences compared with the groups without MH treatment (Figure S20). As shown in Figure S21, no clear damage in visceral and blood indices was observed in the MH group. These results showed great biocompatibility and biosafety of FeM@Sr-TNK NPs and MT in vivo, supporting their great potential in clinical applications.

CONCLUSION

In conclusion, we demonstrated that FeM@Sr-TNK NPs are a comprehensive nanoplatform for the magnetic-response-based rapid diagnosis and treatment of thrombi, and the NPs significantly prolonged the half-life of thrombolytic drugs to 3.04 times that of TNK. Furthermore, these NPs protected the kidney organs by scavenging overexpressed RONS and the therapeutic effects of bioactive ions to prevent RIRI after thrombolysis. By taking full advantage of the rapid targeting and magnetic thermal properties of Fe$_3$O$_4$, the efficient thrombolysis of magnetocaloric combined with TNK was resoundingly verified in vitro and in vivo. Furthermore, the dopamine on the surface of FeM@Sr-TNK NPs exhibits excellent antioxidative activity against various types of toxic RONS as well as the ability of PAI. Moreover, we found that FeM@Sr-TNK NPs can protect renal tissue and promote the activation of blood vessels after RIRI via antiapoptotic effects, increasing angiogenesis factors, and antifibrosis. Therefore, these NPs provide a functional nanoplatform for antithrombotic and antioxidant therapy, reducing side effects and protecting the organization after RIRI, which provides a strategy for treating thrombosis disease and subsequent tissue damage. However, it is worth noting that vascular disease and related organ damage are very large and complex systems. We have explored only the kidneys, and the heart, brain, liver, and other organs are also involved in related problems, which necessitates further study.

EXPERIMENTAL SECTION

Materials. Dopamine hydrochloride (DA·HCl), 1,3,5-trimethylbenzene (TMB) triblock copolymer pluronic F127, H-D-isoleucyl-L-prolyl-L-arginine-p-nitroanilide dihydrochloride (S-2288) and ammonium hydroxide solution were purchased from Sigma−Aldrich Chemical Co. Strontium chloride was obtained from Damas-beta. Ethanol and methanol were purchased from General-Reagent. DCFH-DA and the Reactive Oxygen Species Assay Kit were purchased from Beyotime Biotechnology. TNK-tPA was purchased from Recomgen Biotech. FITC-labeled fibrin was purchased from Qiangyao Biological Technology Co. All other reagents used were of at least analytical grade. Fe_3O_4 was purchased from North China Science and Technology Metal Materials. Griess reagent was obtained from Beijing Yaanda Biotechnology Co., Ltd.

Synthesis of Various NPs. Based on the soft template method and chelation, the entire synthesis process included the following steps: preparation of the precursor (Fe_3O_4@PDA-Sr/F127/TMB) and synthesis of magnetic mesoporous PDA (Fe_3O_4@MPDA-Sr (FeM@Sr NPs)) by refluxing and loading TNK-tPA onto Fe_3O_4@MPDA-Sr to obtain the final Fe_3O_4@MPDA-Sr-TNK (FeM@Sr-TNK NPs).

In the first step according to previous reports,[28] F127 (100 mg) was dispersed in a solution containing H_2O (5 mL) and ethanol (5 mL). Then, TMB (0.16 mL) was injected into the solution with stirring for 30 min. Then, Fe_3O_4 (20 mg), strontium chloride (20 mg), and dopamine hydrochloride (60 mg) were introduced into the solution, and the mixture was sonicated until uniform. Then, $NH_3 \cdot H_2O$ (0.09 mL, 28%) was added to the above solution, and the mixture was stirred for 24 h. Fe_3O_4@PDA-Sr/F127/TMB was separated by centrifugation (11,000 rpm). The synthesis of Fe_3O_4@PDA/F127/TMB did not add strontium chloride, and the other steps were the same.

To synthesize FeM@Sr, the template was removed by the extraction method, in which a mixed solution of ethanol and acetone (2:1 v/v) was sonicated (3 times, 0.5 h each time). FeM NPs were synthesized by the same method.

For the synthesis of FeM@Sr-TNK NPs, the obtained FeM@Sr NPs (20 mg) were mixed with TNK (1.2 mg) in tris buffer (10 mL, pH 8.5) with stirring for 12 h. Then, the final product was obtained by centrifugation (10,000 rpm) and resuspended in distilled water. FeM@Sr-TNK NPs (10 mg) were stirred together with DIR dye (500 μg) for 12 h and then centrifuged to obtain DIR-labeled FeM@Sr-TNK NPs.

Characterization of FeM@Sr-TNK NPs and Related Materials. SEM images were recorded (GeminiSEM 300, ZEISS, Germany). High-resolution morphology and energy spectrum mapping of FeM@Sr-TNK were obtained by TEM (Tecnai G2 F30, FEI, OXFORD, America). The contents of Fe and Sr in the FeM@Sr-TNK NPs and the concentration of Sr^{2+} released from FeM@Sr-TNK NPs at different times (1, 4, 7, 14, 28 d) were measured by an inductively coupled plasma optical emission spectrometer (5110 ICP-OES, Agilent, America). Notably, by the formula $n = m/M$ (amount of substance (n), mass (m), molar mass (M)), and the proportion between the amount of substance of Fe and Fe_3O_4, the content of Fe_3O_4 was obtained. The drug loading rate of TNK in FeM@Sr-TNK NPs was calculated by ELISA (Boster Biological Technology Co., Ltd.) after the NPs were destroyed with DMSO. Nitrogen adsorption−desorption isotherms were tested by an analyzer (ASAP 2460, MicroActive, America). A dynamic laser scattering particle sizer was used to measure the average diameters and ζ potentials (DSL, Brookhaven Instruments, Model ZEN3600, America). The Brunauer−Emmett−Teller method was used to calculate the specific surface area, and the Barrett−Joyner−Halenda method was used to calculate pore size distribution curves. Saturation magnetization values of Fe_3O_4 and FeM@Sr-TNK NPs were measured by a hysteresis loop test (LakeShore 7404, American). The magnetic property of freeze-dried FeM@Sr-TNK NPs was verified by magnet attraction. A dispersive spectrophotometer (LabRAM HR Evolution, Horiba Scientific, Japan) was used to obtain the Raman spectra. FTIR spectra were obtained using an FTIR spectrometer (Nicolet iS20, Thermo Scientific, China). X-ray photoelectron spectroscopy of FeM@Sr NPs was also performed (Thermo Scientific K-Alpha, American). To verify the stability of the NPs, we dispersed the FeM@Sr-TNK NPs in ethanol, observed the state of the NPs at different time points (1, 7, 14, and 28 d), and obtained photos for recording. To evaluate the MH performance of FeM@Sr-TNK NPs, various concentrations of FeM@Sr-TNK NPs (1, 2, 3, 4, and 5 mg mL^{-1}) were stimulated with alternating magnetic fields (SPG-10AB-II, Shuangping Corporation, Shenzhen, China) at specific times (1, 2, 3, 4, 5 min). Additionally, the MH performance of Fe_3O_4 (equivalent to FeM@Sr-TNK NPs), PBS, MPDA and FeM@Sr NPs was tested under the same conditions (5 mg mL^{-1}). An infrared thermal imaging system (Fotric 226, China) was used to record the accordant thermal images.

Targeting and Imaging *In Vitro* and *In Vivo*. To simulate the vascular environment, we designed a vascular model with inner diameters ranging from thick to thin (10, 6, 4, and 2 mm) with different stenosis and torsion degrees to verify the MT capabilities of the FeM@Sr-TNK NPs guided by the magnet. FeM@Sr-TNK NPs (30 mg) were added to the vascular model. The time it took for the NPs to pass through different tube diameters was recorded. The iron content of the FeM@Sr-TNK NPs at the start and end points was detected by ICP, and the delivery rate was analyzed by the following formula: iron content at end point/iron content at starting point × 100%.

To test the PAI performance of FeM@Sr-TNK *in vitro*, FeM@Sr-TNK NP solution was placed into agarose gel models and irradiated with a full-wavelength laser with an excitation wavelength from 680 to 970 nm with a step of 5 nm. Then, a Vevo LAZR System (Visual Sonics Inc., Canada) was used to image the FeM@Sr-TNK NP solution at concentrations from 0.25 to 4 mg mL^{-1} (200 μL).

All animal experiments conformed to the Guide for Animal Ethical Commission of Chongqing Medical University, and the protocols were approved by the Institutional Animal Care Committee of Chongqing Medical University (Ethics number: 2019-078). Sprague−Dawley (SD) rats and Kunming (KM) mice were purchased from the Animal Center of Chongqing Medical University and anesthetized with pentobarbital sodium (1%). The SD rats were anesthetized and fixed, and the right renal artery was exposed. 10% $FeCl_3$-treated 2 mm paper was wrapped around the right renal artery for 10 min to produce an occlusive thrombus, and excess $FeCl_3$ solution was cleaned with saline.

To confirm the PAI ability of FeM@Sr-TNK NPs *in vivo*, NPs were administered to SD rats (1 mL, 5 mg mL^{-1} of NPs). In the targeting group, a magnet was used at the thrombus site according to the modeling position, while in the nontargeted group, a magnet was not used. The PAI of the right renal artery regions was obtained at specific times (0, 5, 10, 15, 20, and 30 min). In addition, the quantitative analysis results were calculated.

Accelerated Thrombolytic Therapy *In Vitro* and *In Vivo*. An infrared thermal imager was used to monitor the temperature during MH processing. The required temperature was maintained by adjusting the power in alternating magnetic fields. To verify the influence of temperature on the release of TNK from FeM@Sr-TNK, the release kinetics of TNK in FeM@Sr-TNK preparations were tested at 37 °C, 40 °C, 43 °C, and 46 °C in alternating magnetic fields. FeM@Sr-TNK (each 4 mg of NPs) was placed in a microtube containing phosphate-buffered saline (PBS; pH 7.4) at different temperatures. At specific times (0.5, 1, 1.5, 2, 3, and 4 h), a certain amount of supernatant was obtained (10,000 rpm at 4 °C for 10 min) to quantify TNK by ELISA and resuspended in fresh PBS. Enzyme activity was studied with S-2288. Tested samples included the free TNK+37 °C in the water bath and FeM@Sr-TNK preparations (each 4 mg NPs) determined at 37 °C, 40 °C, 43 °C, and 46 °C in alternating magnetic fields. As the first step of testing, Tris-NaCl buffers (0.1 mM, 200 μL) were incubated at 37 °C for 3 min, and samples (200 μL) were mixed with Tris-NaCl buffers for 4 min. Then, chromogenic subtract S-2288 (1 mM, 200 μL) was added. After incubation for 30 min, the mixture was transferred to a 96-well plate

for absorbance measurement, and ΔABS/min at 405 nm was calculated.

The blood of SD rats was incubated for 12 h to produce blood clots. Then, the blood clots were divided into the following groups: saline, TNK, FeM@Sr, FeM@Sr+MH, FeM@Sr-TNK, and FeM@Sr-TNK+MH (each containing 4 mg of NPs and an equivalent TNK dose of 60 μg). Then, after 4 h of treatment, 200 μL of supernatant was collected to obtain the absorbance at 540 nm with a microplate reader. In addition, the blood clots were weighed and photographed at specific times (1, 2, 3, and 4 h), and the thrombolytic rate was calculated by (weight before thrombolysis − weight after thrombolysis)/weight before thrombolysis × 100%.

An agar plate method was used to measure fibrin clot lysis. Briefly, agar (200 mg) was added into the buffer mixture (15 mL of Tris-HCl buffer and 5 mL of CaCl$_2$ solution) and heated in a microwave. Fibrinogen dissolved in Tris-HCl buffer (1 mL) and 100 μL of thrombin (25 U) were added. The mixture was evenly distributed in the plastic plate, and gels were obtained at 4 °C after 1 h. Sample wells (0.5 cm) were created on each plate, and 10 μL of fibrinogen solution (0.5 mg mL^{-1}) was added to each sample well. Groups were divided into saline, TNK, FeM@Sr NPs, FeM@Sr NPs+MH, FeM@Sr-TNK NPs, and FeM@Sr-TNK NPs+MH with an equivalent TNK dose of 60 μg. The dissolution of fibrin clots could be evaluated by measuring the area of the lysed zone of each well.

To evaluate the treatment effect of FeM@Sr-TNK on thrombosis *in vivo*, we randomly divided SD rats into seven groups: the thrombosis group, TNK group, FeM@Sr+MT group, FeM@Sr+MT+MH group, FeM@Sr-TNK group, FeM@Sr-TNK + MT group, and FeM@Sr-TNK + MT + MH group (each 4 mg of NPs and an equivalent TNK dose of 60 μg). The SD rats of the above various groups were intravenously treated with PBS, TNK, FeM@Sr, or FeM@Sr-TNK solution, and the applied MT (permanent magnets were placed at the thrombus) with or without MH (the rats were placed in alternating magnetic fields) was used for specific grouping. For the group requiring MH treatment, we placed the rats in the alternating magnetic field to heat for half an hour and then rest for half an hour, and we repeated this process four times. During the process, an infrared thermal imager was continuously used to monitor the temperature of the targeted group and nontargeted group. After 24 h of treatment, H&E staining images of the right renal artery were observed by light microscopy. ImageJ software was used to evaluate the treatment level of the renal artery thrombus and calculated by the following formula: thrombus residual rate % = residual thrombus area/total vascular area × 100%. To measure the temperature of the internal organs, after FeM@Sr-TNK+MT+MH treatment, the rats were immediately laparotomized to observe the temperature of the liver, spleen, and kidneys in alternating magnetic fields.

After intravenous injection of TNK or FeM@Sr-TNK at equal concentrations (each 4 mg of NPs and an equivalent TNK dose of 60 μg) in healthy SD rats, 0.5 mL of blood was collected from each rat at 10, 20, 30, 60, 90, and 120 min. Microcentrifuge tubes were used to collect blood samples, and then, the plasma was separated by centrifugation (4000 rpm for 10 min). The amidolytic activity method was used to verify the residual activity of the TNK.

To further clarify the site of thrombolysis by FeM@Sr-TNK NPs, 20 μL of thrombin (25 U mL^{-1}) was added to the mixed solution containing 200 μL of CaCl$_2$ (2.5 mM) and 200 μL of FITC-labeled fibrinogen (10 mg mL^{-1}) to obtain fibrin clots and then washed several times with PBS. The fibrin clots were treated as follows: saline, TNK, FeM@Sr NPs, FeM@Sr NPs+MH, FeM@Sr-TNK NPs, and FeM@Sr-TNK NPs+MH (43 °C) (each 4 mg of NPs and an equivalent TNK dose of 60 μg). Then, a fluorescence microscope was used to observe the structure of FITC-labeled fibrin clots

RONS Scavenging *In Vitro* and at the Thrombus Site. To test the capacity of NPs to scavenge RONS *in vitro*, the DPPH free radical scavenging activity and SOD-like enzyme activity were tested by a detection kit (Solarbio Science & Technology Co., Ltd. Beijing, China).

To verify the ability of NPs to scavenge RONS at the cellular level, HEK293 cells were seeded into a 96-well plate (10^4 cells per well) and

incubated for 24 h. DHE and DCFH-DA were used to evaluate the intracellular superoxide anion level and the amount of a variety of ROS, respectively. Briefly, HEK293 cells were cultured in a normal or ROS microenvironment induced by H$_2$O$_2$ with different FeM@Sr-TNK concentrations (100 μL, 0, 0.1, 0.2, 0.3, 0.4, and 0.5 mg mL^{-1}). DHE or DCFH-DA was used with cells for 15−25 min in the dark, which were observed under a fluorescence microscope, and then the fluorescence intensity.

Griess reagent was used to determine the NO scavenging capacity. Five ×10^5 cells/well in 100 μL of HEK293 was added into a 96-well plate for 24 h. 100 μg/mL LPS and different concentrations of FeM@Sr-TNK NPs (100 μL, 1, 5, and 10 mg mL^{-1}) costimulated cells for 24 h. After treatments, the supernatants were collected and analyzed for nitrite amounts using 10 μL/well Griess reagent. The absorbance at a wavelength of 548 nm was determined with a microplate reader. The yield of nitrite was quantitatively analyzed according to the standard curve equation: $y = 0.001996x + 0.06975$ (y is absorbance and x is the concentration of nitrite (1−100 μM)). After the different treatments described above, the cell viabilities were determined by CCK8 analysis.

To verify the ability of NPs to scavenge ROS at the thrombus site, right renal arteries were excised from rats 24 h after treatment and cut into tissue sections. The samples were divided into five groups: the thrombosis group, TNK group, FeM@Sr-TNK group, FeM@Sr-TNK +MT group, and FeM@Sr-TNK+MT+MH group (each 4 mg of NPs and an equivalent TNK dose of 60 μg). The ROS content was detected by DHE staining and fluorescence microscopy, and the intensity of the ROS fluorescence was analyzed with ImageJ.

RIRI Treatment *In Vivo*: RONS Scavenging in the Kidney Protects Renal Tubules and Improves Renal Function. We referenced previous research to establish the IRIR model.[69,70] As illustrated in Figure 6a, all female mice were provided food but no water for 18 h, after which both hind limbs were intramuscularly (i.m.) injected with 50% glycerol (8 mL kg^{-1}). Subsequently, all mice returned to a normal feeding mode. At 2 h postinjection, the RIRI model was established and used for the next study.

To verify the therapeutic effect of FeM@Sr-TNK NPs, we divided the mice into the following groups: group 1 included healthy mice treated with 200 μL of 1 × PBS; group 2 included healthy mice treated with 800 μL of FeM@Sr-TNK (high dose); group 3 included RIRI mice treated with 200 μL of 1 × PBS; group 4 included RIRI mice treated with 200 μL of FeM@Sr-TNK (low dose); and group 5 included RIRI mice treated with 800 μL of FeM@Sr-TNK (high dose). These mice were given the agents intravenously (4 mg mL^{-1} of FeM@Sr-TNK NPs).

The therapeutic efficacy of FeM@Sr-TNK NPs in the RIRI model was evaluated by RONS scavenging, pathological slides, and renal function. The blood and kidneys of the mice were collected 24 h after the injection of the agent. The frozen kidneys were further cut into tissue slices and stained with DHE, and a fluorescence microscope was used for observations and to take photos. The collected kidneys were used for sectioning and H&E staining. Pediatric heparin tubes were used to collect blood samples, and after centrifugation (2000 rpm for 15 min at 4 °C), the plasma was collected. Plasma renal function indicators containing BUN and CRE were analyzed.

Bioactive Ion Therapy *In Vivo*: Reducing Apoptosis, Increasing Angiogenesis, and Inhibiting Fibrosis. The KM mice were divided into three groups: RIRI mice, RIRI mice+FeM-TNK, and RIRI mice+FeM@Sr-TNK (800 μL, 4 mg mL^{-1} of FeM@Sr-TNK NPs). In addition, the Western blot (WB) analysis added an additional group of healthy mice, while the other treatments were consistent with the above. The mouse kidneys were collected and washed with PBS and embedded in OCT compound for frozen sectioning. Then, the tissues were cut for TUNEL staining. The tissue was digested with tissue lysis buffer, and the protein supernatant was collected by centrifugation (11,000 rpm for 30 min at 4 °C). WB analysis was carried out, and antibodies against total/cleaved caspase-3 (Cell Signaling Technology, 9662), Bcl-2 (Beyotime Technology, AB112), and Bax (Abcam, ab32503) were used for analysis. The tissues were cut for immunofluorescence staining, including α-SMA,

CD31, and VEGF, and Masson's trichrome staining with the same treatment after 28 d. The concentrations of Sr^{2+} ions in kidneys collected on the 1st, 7th, 14th, and 28th days after IRIR were studied by inductively coupled plasma-mass spectrometry (ICP-MS; Agilent 7700, USA).

Biodistribution and Biosafety Assessment. To certify the DIR-FeM@Sr-TNK *in vitro* fluorescence intensity, we used concentrations ranging from 0.625 mg mL^{-1} to 10 mg mL^{-1} (1 mL) to obtain FLI by an imaging system (IVIS, PerkinElmer, U.K.). To study the biological distribution of DIR-FeM@Sr-TNK *in vivo*, we injected 200 μL of DIR-FeM@Sr-TNK (5 mg mL^{-1}) into KM mice, and major organs (heart, liver, spleen, lungs, and kidneys) were collected for FLI after 24 h.

The blood (5 mL) of rats was added to an appropriate saline solution, shaken well, and centrifuged at 2500 rpm for 5 min. Then, the supernatant was removed, and the sediment was washed three or four times with the above method until the supernatant displayed clarification. The obtained precipitate was prepared as a 2% suspension with saline and divided into seven groups. Groups 1−5 were the drug groups (1, 2, 3, 4, 5 mg mL^{-1}, 200 μL), group 6 (saline) was the negative group, and group 7 (water) was the positive group. After taking photos and storing for 12 h at 4 °C, the supernatant of each tube was centrifuged at 13000 rpm, and then the absorption of the supernatant at 540 nm was determined. The hemolysis rate was calculated. The cells were placed in 96-well plates (2 × 10^4 cells well^{-1}) and incubated until they reached 60% confluence. FeM@Sr-TNK was added at various concentrations (0.1, 0.2, 0.3, 0.4, and 0.5 mg mL^{-1}) for 12 and 24 h, and the medium was discarded at a specific point in time. The medium containing CCK8 reagent was added, and the mixture was incubated at 37 °C for 2 h. Then, the absorbance of the above medium was determined with a microplate reader (Bio-Tek Instrument Inc., USA) at a wavelength of 450 nm.

To evaluate the effect of FeM@Sr-TNK on hemostasis, a tail bleeding test on KM mice (female, 6−8 weeks) was used. We randomly divided the mice into three groups ($n = 3$): PBS, TNK, and FeM@Sr-TNK (each 800 μL, 4 mg mL^{-1} NPs). After 30 min of treatment, the tip of the tail of the mice was cut off by 1 cm. When the blood overflowed automatically, we counted the time and used gauze to absorb the blood once every 10 s. The time at which blood flow stopped was recorded, and the bleeding time of the mice was calculated. The blood clotting time was measured using the slide method. One h after administration (PBS, FeM, FeM@Sr, and FeM@Sr-TNK), the left eye of the mouse was removed with tweezers. Blood was taken from the posterior venous plexus of the left eye. After the first drop of blood was wiped off, a drop of blood was dropped on the slide while waiting at the same time. A clean needle was used to place blood filaments on the slide every 30 s. When blood filaments appeared, the timing was completed, and the blood clotting time was obtained.

Into 20 healthy KM mice, 200 μL of FeM@Sr-TNK solution (6 mg mL^{-1}) was injected. Five healthy mice treated with saline served as the control group. Mouse retroorbital blood was collected at different points in time (1, 4, 7, 14 d) for hematological analysis. Finally, after sacrifice, the main organs were stained with H&E for pathological analysis.

In addition, by observing the histological sections of renal artery vessels with thrombi after different treatments, it could be verified whether different treatments would cause damage to the blood vessel wall. To determine whether MH would cause damage to organs, rats were divided into three groups: PBS, FeM@Sr-TNK, and FeM@Sr-TNK+MH. After treatment, rat blood was collected for hematological analysis, and H&E staining of the main organs was used for pathological analysis.

Statistical Analysis. Data are presented as the mean ± the standard deviation. Statistical analysis was conducted using one-way ANOVA or t test by GraphPad Prism software, version 7.0. ns: not significant, *$p < 0.05$, **$p < 0.01$, ***$p < 0.001$, ****$p < 0.0001$ were considered statistically significant in the analyses.

ASSOCIATED CONTENT

ⓈⒾ Supporting Information

The Supporting Information is available free of charge at https://pubs.acs.org/doi/10.1021/acsnano.2c12091.

Experimental extra data: elemental line-scan mapping, size distribution and ζ potentials, N_2 adsorption—desorption isotherms, XPS, stability in ethanol, temperature changes in alternating magnetic fields, quantitative analysis of signal intensity, analysis of the supernatant after thrombolysis, images and quantitative analysis of the fibrin clots, temperature images of targeted and nontargeted groups, quantitative analysis of the thrombosis residual rate, the temperature of the liver, spleen and kidney, pictures of the colors resulting from reactions, nitric oxide scavenging activity, relative cell viabilities, the ROS fluorescence intensity, the concentrations of Sr^{2+} in kidneys, the hemolysis rate of red blood cells, bleeding assay and coagulation assay, H&E staining of renal arteries, biosafety assessment for MH treatment (PDF)

AUTHOR INFORMATION

Corresponding Authors

Jie Xu − *Department of Radiology, Second Affiliated Hospital of Chongqing Medical University, Chongqing 400010, PR China;* ⓞ orcid.org/0000-0002-2523-7915; Email: Xujie321@126.com

Dajing Guo − *Department of Radiology, Second Affiliated Hospital of Chongqing Medical University, Chongqing 400010, PR China;* ⓞ orcid.org/0000-0001-8655-6621; Email: guodaj@163.com

Authors

Lian Xu − *Department of Radiology and Chongqing Key Laboratory of Ultrasound Molecular Imaging and Department of Ultrasound, Second Affiliated Hospital of Chongqing Medical University, Chongqing 400010, PR China; State Key Laboratory of Ultrasound in Medicine and Engineering, Chongqing Medical University, Chongqing 400016, PR China*

Ying Luo − *Department of Radiology, Second Affiliated Hospital of Chongqing Medical University, Chongqing 400010, PR China*

Qianying Du − *Department of Radiology, Second Affiliated Hospital of Chongqing Medical University, Chongqing 400010, PR China*

Wenli Zhang − *Department of Radiology, Second Affiliated Hospital of Chongqing Medical University, Chongqing 400010, PR China*

Liu Hu − *Department of Radiology, Second Affiliated Hospital of Chongqing Medical University, Chongqing 400010, PR China*

Ni Fang − *Department of Radiology, Second Affiliated Hospital of Chongqing Medical University, Chongqing 400010, PR China*

Junrui Wang − *Department of Radiology, Second Affiliated Hospital of Chongqing Medical University, Chongqing 400010, PR China*

Jia Liu − *Department of Radiology, Second Affiliated Hospital of Chongqing Medical University, Chongqing 400010, PR China*

Jun Zhou − *Department of Radiology, Second Affiliated Hospital of Chongqing Medical University, Chongqing 400010, PR China*

Yixin Zhong − *Department of Radiology, Second Affiliated Hospital of Chongqing Medical University, Chongqing 400010, PR China*

Yun Liu − *Department of Radiology, Second Affiliated Hospital of Chongqing Medical University, Chongqing 400010, PR China*

Haitao Ran − *Chongqing Key Laboratory of Ultrasound Molecular Imaging and Department of Ultrasound, Second Affiliated Hospital of Chongqing Medical University, Chongqing 400010, PR China;* ⊙ orcid.org/0000-0002-3820-1970

Complete contact information is available at:
https://pubs.acs.org/10.1021/acsnano.2c12091

Notes

ACKNOWLEDGMENTS

REFERENCES

(1) Xu, J.; Zhang, Y.; Xu, J.; Liu, G.; Di, C.; Zhao, X.; Li, X.; Li, Y.; Pang, N.; Yang, C.; Li, Y.; Li, B.; Lu, Z.; Wang, M.; Dai, K.; Yan, R.; Li, S.; Nie, G. Engineered Nanoplatelets for Targeted Delivery of Plasminogen Activators to Reverse Thrombus in Multiple Mouse Thrombosis Models. *Adv. Mater.* 2020, 32, e1905145.

(2) Absar, S.; Gupta, N.; Nahar, K.; Ahsan, F. Engineering of Plasminogen Activators for Targeting to Thrombus and Heightening Thrombolytic Efficacy. *J. Thromb. Haemost.* 2015, 13, 1545−1556.

(3) Chen, W.; Li, D. Reactive Oxygen Species (ROS)-Responsive Nanomedicine for Solving Ischemia-Reperfusion Injury. *Front. Chem.* 2020, 8, 732.

(4) Lu, Y.; Li, C.; Chen, Q.; Liu, P.; Guo, Q.; Zhang, Y.; Chen, X.; Zhang, Y.; Zhou, W.; Liang, D.; Zhang, Y.; Sun, T.; Lu, W.; Jiang, C. Microthrombus-Targeting Micelles for Neurovascular Remodeling and Enhanced Microcirculatory Perfusion in Acute Ischemic Stroke. *Adv. Mater.* 2019, 31, e1808361.

(5) Huang, T.; Li, N.; Gao, J. Recent Strategies on Targeted Delivery of Thrombolytics. *Asian J. Pharm. Sci.* 2019, 14, 233−247.

(6) Su, M.; Dai, Q.; Chen, C.; Zeng, Y.; Chu, C.; Liu, G. Nano-Medicine for Thrombosis: a Precise Diagnosis and Treatment Strategy. *Nanomicro Lett.* 2020, 12, 96.

(7) Zhou, J.; Guo, D.; Zhang, Y.; Wu, W.; Ran, H.; Wang, Z. Construction and Evaluation of Fe^{34}-Based PLGA Nanoparticles Carrying rtPA Used in the Detection of Thrombosis and in Targeted Thrombolysis. *ACS Appl. Mater. Interfaces* 2014, 6, 5566−5576.

(8) Xu, J.; Zhou, J.; Zhong, Y.; Zhang, Y.; Liu, J.; Chen, Y.; Deng, L.; Sheng, D.; Wang, Z.; Ran, H.; Guo, D. Phase Transition Nanoparticles as Multimodality Contrast Agents for the Detection of Thrombi and for Targeting Thrombolysis: in Vitro and in Vivo Experiments. *ACS Appl. Mater. Interfaces* 2017, 9, 42525−42535.

(9) Xu, J.; Zhou, J.; Zhong, Y.; Zhang, Y.; Ye, M.; Hou, J.; Wang, Z.; Ran, H.; Liu, J.; Guo, D. EWVDV-Mediated Platelet-Targeting

(10) Zhong, Y.; Zhang, Y.; Xu, J.; Zhou, J.; Liu, J.; Ye, M.; Zhang, L.; Qiao, B.; Wang, Z. G.; Ran, H. T.; Guo, D. Low-Intensity Focused Ultrasound-Responsive Phase-Transitional Nanoparticles for Thrombolysis Without Vascular Damage: a Synergistic Nonpharmaceutical Strategy. *ACS Nano* 2019, 13, 3387−3403.

(11) Wang, S.; Guo, X.; Xiu, W.; Liu, Y.; Ren, L.; Xiao, H.; Yang, F.; Gao, Y.; Xu, C.; Wang, L. Accelerating Thrombolysis Using a Precision and Plot-Penetrating Drug Delivery Strategy by Nanoparticle-Shelled Microbubbles. *Sci. Adv.* 2020, 6, eaaz8204.

(12) Wan, M.; Wang, Q.; Wang, R.; Wu, R.; Li, T.; Fang, D.; Huang, Y.; Yu, Y.; Fang, L.; Wang, X.; Zhang, Y.; Miao, Z.; Zhao, B.; Wang, F.; Mao, C.; Jiang, Q.; Xu, X.; Shi, D. Platelet-Derived Porous Nanomotor for Thrombus Therapy. *Sci. Adv.* 2020, 6, eaaz9014.

(13) Cheng, R.; Huang, W.; Huang, L.; Yang, B.; Mao, L.; Jin, K.; ZhuGe, Q.; Zhao, Y. Acceleration of Tissue Plasminogen Activator-Mediated Thrombolysis by Magnetically Powered Nanomotors. *ACS Nano* 2014, 8, 7746−7754.

(14) Sitti, M.; Wiersma, D. S. Pros and Cons: Magnetic Versus Optical Microrobots. *Adv. Mater.* 2020, 32, e1906766.

(15) Ma, Y. H.; Wu, S. Y.; Wu, T.; Chang, Y. J.; Hua, M. Y.; Chen, J. P. Magnetically Targeted Thrombolysis with Recombinant Tissue Plasminogen Activator Bound to Polyacrylic Acid-Coated Nanoparticles. *Biomaterials* 2009, 30, 3343−3351.

(16) Singh, A.; Jain, S.; Sahoo, S. K. Magnetic Nanoparticles for Amalgamation of Magnetic Hyperthermia and Chemotherapy: an Approach Towards Enhanced Attenuation of Tumor. *Mater. Sci. Eng. C Mater. Biol. Appl.* 2020, 110, 110695.

(17) Jose, J.; Kumar, R.; Harilal, S.; Mathew, G. E.; Parambi, D. G. T.; Prabhu, A.; Uddin, M. S.; Aleya, L.; Kim, H.; Mathew, B. Magnetic Nanoparticles for Hyperthermia in Cancer Treatment: an Emerging Tool. *Environ. Sci. Pollut. Res. Int.* 2020, 27, 19214−19225.

(18) Liu, C. H.; Hsu, H. L.; Chen, J. P.; Wu, T.; Ma, Y. H. Thrombolysis Induced by Intravenous Administration of Plasminogen Activator in Magnetoliposomes: Dual Targeting by Magnetic and Thermal Manipulation. *Nanomedicine* 2019, 20, 101992.

(19) Voros, E.; Cho, M.; Ramirez, M.; Palange, A. L.; De Rosa, E.; Key, J.; Garami, Z.; Lumsden, A. B.; Decuzzi, P. TPA Immobilization on Iron Oxide Nanocubes and Localized Magnetic Hyperthermia Accelerate Blood Clot Lysis. *Adv. Funct. Mater.* 2015, 25, 1709−1718.

(20) Zenych, A.; Fournier, L.; Chauvierre, C. Nanomedicine Progress in Thrombolytic Therapy. *Biomaterials* 2020, 258, 120297.

(21) Zhao, T.; Wu, W.; Sui, L.; Huang, Q.; Nan, Y.; Liu, J.; Ai, K. Reactive Oxygen Species-Based Nanomaterials for the Treatment of Myocardial Ischemia Reperfusion Injuries. *Bioact. Mater.* 2022, 7, 47−72.

(22) Yang, B.; Chen, Y.; Shi, J. Reactive Oxygen Species (ROS)-Based Nanomedicine. *Chem. Rev.* 2019, 119, 4881−4985.

(23) Yang, B.; Yao, H.; Yang, J.; Chen, C.; Shi, J. Construction of a Two-Dimensional Artificial Antioxidase for Nanocatalytic Rheumatoid Arthritis Treatment. *Nat. Commun.* 2022, 13, 1988.

(24) Mei, T.; Kim, A.; Vong, L. B.; Marushima, A.; Puentes, S.; Matsumaru, Y.; Matsumura, A.; Nagasaki, Y. Encapsulation of Tissue Plasminogen Activator in pH-Sensitive Self-Assembled Antioxidant Nanoparticles for Ischemic Stroke Treatment - Synergistic Effect of Thrombolysis and Antioxidant. *Biomaterials* 2019, 215, 119209.

(25) Liu, Y.; Ai, K.; Ji, X.; Askhatova, D.; Du, R.; Lu, L.; Shi, J. Comprehensive Insights into the Multi-Antioxidative Mechanisms of Melanin Nanoparticles and Their Application to Protect Brain from Injury in Ischemic Stroke. *J. Am. Chem. Soc.* 2017, 139, 856−862.

(26) Qi, C.; Fu, L.-H.; Xu, H.; Wang, T.-F.; Lin, J.; Huang, P. Melanin/Polydopamine-Based Nanomaterials for Biomedical Applications. *Science China Chemistry* 2019, 62, 162−188.

(27) Yu, W.; Yin, N.; Yang, Y.; Xuan, C.; Liu, X.; Liu, W.; Zhang, Z.; Zhang, K.; Liu, J.; Shi, J. Rescuing Ischemic Stroke by Biomimetic Nanovesicles through Accelerated Thrombolysis and Sequential Ischemia-Reperfusion Protection. *Acta Biomater.* 2022, 140, 625−640.

(28) Zhao, H.; Zeng, Z.; Liu, L.; Chen, J.; Zhou, H.; Huang, L.; Huang, J.; Xu, H.; Xu, Y.; Chen, Z.; Wu, Y.; Guo, W.; Wang, J.; Wang, J.; Liu, Z. Polydopamine Nanoparticles for the Treatment of Acute Inflammation-Induced Injury. *Nanoscale* **2018**, *10*, 6981−6991.

(29) Sun, T.; Jiang, D.; Rosenkrans, Z. T.; Ehlerding, E. B.; Ni, D.; Qi, C.; Kutyreff, C. J.; Barnhart, T. E.; Engle, J. W.; Huang, P.; Cai, W. A Melanin-Based Natural Antioxidant Defense Nanosystem for Theranostic Application in Acute Kidney Injury. *Adv. Funct. Mater.* **2019**, *29*, 1904833.

(30) Battaglini, M.; Marino, A.; Carmignani, A.; Tapeinos, C.; Cauda, V.; Ancona, A.; Garino, N.; Vighetto, V.; La Rosa, G.; Sinibaldi, E.; Ciofani, G. Polydopamine Nanoparticles as an Organic and Biodegradable Multitasking Tool for Neuroprotection and Remote Neuronal Stimulation. *ACS Appl. Mater. Interfaces* **2020**, *12*, 35782−35798.

(31) Wang, Z.; Zou, Y.; Li, Y.; Cheng, Y. Metal-Containing Polydopamine Nanomaterials: Catalysis, Energy, and Theranostics. *Small* **2020**, *16*, e1907042.

(32) Pu, Y.; Zhu, Y.; Qiao, Z.; Xin, N.; Chen, S.; Sun, J.; Jin, R.; Nie, Y.; Fan, H. A Gd-Doped Polydopamine (PDA)-Based Theranostic Nanoplatform as a Strong MR/PA Dual-Modal Imaging Agent for PTT/PDT Synergistic Therapy. *J. Mater. Chem. B* **2021**, *9*, 1846−1857.

(33) Cheng, W.; Zeng, X.; Chen, H.; Li, Z.; Zeng, W.; Mei, L.; Zhao, Y. Versatile Polydopamine Platforms: Synthesis and Promising Applications for Surface Modification and Advanced Nanomedicine. *ACS Nano* **2019**, *13*, 8537−8565.

(34) Xie, X.; Tang, J.; Xing, Y.; Wang, Z.; Ding, T.; Zhang, J.; Cai, K. Intervention of Polydopamine Assembly and Adhesion on Nanoscale Interfaces: State-of-the-Art Designs and Biomedical Applications. *Adv. Healthc. Mater.* **2021**, *10*, e2002138.

(35) Jin, A.; Wang, Y.; Lin, K.; Jiang, L. Nanoparticles Modified by Polydopamine: Working as "Drug" Carriers. *Bioact. Mater.* **2020**, *5*, 522−541.

(36) Chen, F.; Xing, Y.; Wang, Z.; Zheng, X.; Zhang, J.; Cai, K. Nanoscale Polydopamine (PDA) Meets π-π Interactions: an Interface-Directed Coassembly Approach for Mesoporous Nanoparticles. *Langmuir* **2016**, *32*, 12119−12128.

(37) Tao, C.; Chen, T.; Liu, H.; Su, S. Design of Biocompatible Fe_3O_4@MPDA Mesoporous Core-Shell Nanospheres for Drug Delivery. *Microporous Mesoporous Mater.* **2020**, *293*, 109823.

(38) Shu, G.; Chen, M.; Song, J.; Xu, X.; Lu, C.; Du, Y.; Xu, M.; Zhao, Z.; Zhu, M.; Fan, K.; Fan, X.; Fang, S.; Tang, B.; Dai, Y.; Du, Y.; Ji, J. Sialic Acid-Engineered Mesoporous Polydopamine Nanoparticles Loaded with SPIO and Fe (3+) as a Novel Theranostic Agent for T1/T2 Dual-Mode MRI-Guided Combined Chemo-Photothermal Treatment of Hepatic Cancer. *Bioact. Mater.* **2021**, *6*, 1423−1435.

(39) Xu, Z.; Wu, Y.; Wu, H.; Sun, N.; Deng, C. Hydrophilic Polydopamine-Derived Mesoporous Channels for Loading Ti(IV) Ions for Salivary Phosphoproteome Research. *Anal. Chim. Acta* **2021**, *1146*, 53−60.

(40) Lin, L. S.; Cong, Z. X.; Cao, J. B.; Ke, K. M.; Peng, Q. L.; Gao, J.; Yang, H. H.; Liu, G.; Chen, X. Multifunctional Fe_3O_4@polydopamine Core-Shell Nanocomposites for Intracellular mRNA Detection and Imaging-Guided Photothermal Therapy. *ACS Nano* **2014**, *8*, 3876−3883.

(41) Pan, P.; Zhang, T.; Yue, Q.; Elzatahry, A. A.; Alghamdi, A.; Cheng, X.; Deng, Y. Interface Coassembly and Polymerization on Magnetic Colloids: Toward Core-Shell Functional Mesoporous Polymer Microspheres and Their Carbon Derivatives. *Adv. Sci.* **2020**, *7*, 2000443.

(42) Wan, D.; Yan, C.; Zhang, Q. Facile and Rapid Synthesis of Hollow Magnetic Mesoporous Polydopamine Nanoflowers with Tunable Pore Structures for Lipase Immobilization: Green Production of Biodiesel. *Ind. Eng. Chem. Res.* **2019**, *58*, 16358−16369.

(43) Zhao, Y.; Zhang, Z.; Pan, Z.; Liu, Y. Advanced Bioactive Nanomaterials for Biomedical Applications. *Exploration* **2021**, *1*, 20210089.

(44) Williams, D. F. Biocompatibility Pathways and Mechanisms for Bioactive Materials: the Bioactivity Zone. *Bioact. Mater.* **2022**, *10*, 306−322.

(45) Zhu, H.; Zheng, K.; Boccaccini, A. R. Multi-Functional Silica-Based Mesoporous Materials for Simultaneous Delivery of Biologically Active Ions and Therapeutic Biomolecules. *Acta Biomater.* **2021**, *129*, 1−17.

(46) Vallet-Regi, M.; Salinas, A. J. Mesoporous Bioactive Glasses for Regenerative Medicine. *Mater. Today Bio* **2021**, *11*, 100121.

(47) Hoppe, A.; Guldal, N. S.; Boccaccini, A. R. A Review of the Biological Response to Ionic Dissolution Products from Bioactive Glasses and Glass-Ceramics. *Biomaterials* **2011**, *32*, 2757−2774.

(48) Zhou, Y.; Wu, C.; Chang, J. Bioceramics to Regulate Stem Cells and Their Microenvironment for Tissue Regeneration. *Mater. Today* **2019**, *24*, 41−56.

(49) Yi, M.; Li, H.; Wang, X.; Yan, J.; Gao, L.; He, Y.; Zhong, X.; Cai, Y.; Feng, W.; Wen, Z.; Wu, C.; Ou, C.; Chang, J.; Chen, M. Ion Therapy: a Novel Strategy for Acute Myocardial Infarction. *Adv. Sci. (Weinh)* **2019**, *6*, 1801260.

(50) Mao, L.; Xia, L.; Chang, J.; Liu, J.; Jiang, L.; Wu, C.; Fang, B. The Synergistic Effects of Sr and Si Bioactive Ions on Osteogenesis, Osteoclastogenesis and Angiogenesis for Osteoporotic Bone Regeneration. *Acta Biomater.* **2017**, *61*, 217−232.

(51) Xing, M.; Jiang, Y.; Bi, W.; Gao, L.; Zhou, Y. L.; Rao, S. L.; Ma, L. L.; Zhang, Z. W.; Yang, H. T.; Chang, J. Strontium Ions Protect Hearts Against Myocardial Ischemia/Reperfusion Injury. *Sci. Adv.* **2021**, *7*, eabe0726.

(52) Lin, K.; Gan, Y.; Zhu, P.; Li, S.; Lin, C.; Yu, S.; Zhao, S.; Shi, J.; Li, R.; Yuan, J. Hollow Mesoporous Polydopamine Nanospheres: Synthesis, Biocompatibility and Drug Delivery. *Nanotechnology* **2021**, *32*, No. 285602.

(53) Yang, M.; Zhang, N.; Zhang, T.; Yin, X.; Shen, J. Fabrication of Doxorubicin-Gated Mesoporous Polydopamine Nanoplatforms for Multimode Imaging-Guided Synergistic Chemophotothermal Therapy of Tumors. *Drug Delivery* **2020**, *27*, 367−377.

(54) Huang, X.; Chen, L.; Lin, Y.; Tou, K. I.; Cai, H.; Jin, H.; Lin, W.; Zhang, J.; Cai, J.; Zhou, H.; Pi, J. Tumor Targeting and Penetrating Biomimetic Mesoporous Polydopamine Nanoparticles Facilitate Photothermal Killing and Autophagy Blocking for Synergistic Tumor Ablation. *Acta Biomater.* **2021**, *136*, 456−472.

(55) Guo, H.; Wang, L.; Wu, W.; Guo, M.; Yang, L.; Zhang, Z.; Cao, L.; Pu, F.; Huang, X.; Shao, Z. Engineered Biomimetic Nanoreactor for Synergistic Photodynamic-Chemotherapy Against Hypoxic Tumor. *J. Controlled Release* **2022**, *351*, 151−163.

(56) Ma, J.-X.; Yang, H.; Li, S.; Ren, R.; Li, J.; Zhang, X.; Ma, J. Well-Dispersed Graphene-Polydopamine-Pd Hybrid with Enhanced Catalytic Performance. *RSC Adv.* **2015**, *5*, 97520−97527.

(57) Mallinson, D.; Mullen, A. B.; Lamprou, D. A. Probing Polydopamine Adhesion to Protein and Polymer Films: Microscopic and Spectroscopic Evaluation. *J. Mater. Sci.* **2018**, *53*, 3198−3209.

(58) Farea, M. O.; Abdelghany, A. M.; Meikhail, M. S.; Oraby, A. H. Effect of Cesium Bromide on the Structural, Optical, Thermal and Electrical Properties of Polyvinyl Alcohol and Polyethylene Oxide. *Journal of Materials Research and Technology* **2020**, *9*, 1530−1538.

(59) Jia, Z.; Hao, S.; Cheng, X.; Lu, X.; Tu, L. Fabrication of Prussian Blue/Polydopamine Layers on Polyacrylonitrile Membranes for Efficient Adsorption of Cesium. *Desalination and Water Treatment* **2019**, *163*, 125−132.

(60) Li, B.; Gong, T.; Xu, N.; Cui, F.; Yuan, B.; Yuan, Q.; Sun, H.; Wang, L.; Liu, J. Improved Stability and Photothermal Performance of Polydopamine-Modified Fe_3O_4 Nanocomposites for Highly Efficient Magnetic Resonance Imaging-Guided Photothermal Therapy. *Small* **2020**, *16*, e2003969.

(61) Zhang, L.; Yang, P.; Guo, R.; Sun, J.; Xie, R.; Yang, W. Multifunctional Mesoporous Polydopamine with Hydrophobic Paclitaxel for Photoacoustic Imaging-Guided Chemo-Photothermal Synergistic Therapy. *Int. J. Nanomedicine* **2019**, *14*, 8647−8663.

(62) Tang, Z.; Li, D.; Wang, X.; Gong, H.; Luan, Y.; Liu, Z.; Brash, J. L.; Chen, H. A t-PA/Nanoparticle Conjugate with Fully Retained

Enzymatic Activity and Prolonged Circulation Time. *J. Mater. Chem. B* **2015**, *3*, 977−982.

(63) Campbell, B. C. V.; Mitchell, P. J.; Churilov, L.; Yassi, N.; Kleinig, T. J.; Dowling, R. J.; Yan, B.; Bush, S. J.; Dewey, H. M.; Thijs, V.; Scroop, R.; Simpson, M.; Brooks, M.; Asadi, H.; Wu, T. Y.; Shah, D. G.; Wijeratne, T.; Ang, T.; Miteff, F.; Levi, C. R.; et al. Tenecteplase Versus Alteplase Before Thrombectomy for Ischemic Stroke. *N. Engl. J. Med.* **2018**, *378*, 1573−1582.

(64) Lippi, G.; Mattiuzzi, C.; Favaloro, E. J. Novel and Emerging Therapies: Thrombus-Targeted Fibrinolysis. *Semin. Thromb. Hemost.* **2013**, *39*, 48−58.

(65) Münzel, T.; Gori, T.; Keaney, J. F.; Maack, C.; Daiber, A. Pathophysiological Role of Oxidative Stress in Systolic and Diastolic Heart Failure and Its Therapeutic Implications. *European Heart Journal* **2015**, *36*, 2555−2564.

(66) Zhao, Y.; Xie, R.; Yodsanit, N.; Ye, M.; Wang, Y.; Gong, S. Biomimetic Fibrin-Targeted and H_2O_2-Responsive Nanocarriers for Thrombus Therapy. *Nano Today* **2020**, *35*, 100986.

(67) Ni, D.; Wei, H.; Chen, W.; Bao, Q.; Rosenkrans, Z. T.; Barnhart, T. E.; Ferreira, C. A.; Wang, Y.; Yao, H.; Sun, T.; Jiang, D.; Li, S.; Cao, T.; Liu, Z.; Engle, J. W.; Hu, P.; Lan, X.; Cai, W. Ceria Nanoparticles Meet Hepatic Ischemia-Reperfusion Injury: the Perfect Imperfection. *Adv. Mater.* **2019**, *31*, e1902956.

(68) Zhai, M.; Li, B.; Duan, W.; Jing, L.; Zhang, B.; Zhang, M.; Yu, L.; Liu, Z.; Yu, B.; Ren, K.; Gao, E.; Yang, Y.; Liang, H.; Jin, Z.; Yu, S. Melatonin Ameliorates Myocardial Ischemia Reperfusion Injury through SIRT3-Dependent Regulation of Oxidative Stress and Apoptosis. *J. Pineal Res.* **2017**, *63*, e12419.

(69) Jiang, D.; Ge, Z.; Im, H. J.; England, C. G.; Ni, D.; Hou, J.; Zhang, L.; Kutyreff, C. J.; Yan, Y.; Liu, Y.; Cho, S. Y.; Engle, J. W.; Shi, J.; Huang, P.; Fan, C.; Yan, H.; Cai, W. DNA Origami Nanostructures Can Exhibit Preferential Renal Uptake and Alleviate Acute Kidney Injury. *Nat. Biomed. Eng.* **2018**, *2*, 865−877.

(70) Hou, J.; Wang, H.; Ge, Z.; Zuo, T.; Chen, Q.; Liu, X.; Mou, S.; Fan, C.; Xie, Y.; Wang, L. Treating Acute Kidney Injury with Antioxidative Black Phosphorus Nanosheets. *Nano Lett.* **2020**, *20*, 1447−1454.

📖 Recommended by ACS